Draft version October 6, 2026
Typeset using LaTeX **twocolumn** style in AASTeX631

arXiv:2610.06680v1 [astro-ph.GA] 5 Oct 2026

Unveiling the Origins of the Molecular Gas Reservoirs in Recently Quenched Massive Galaxies

Ethan Savitch (esavitch@ufl.edu) [1], Desika Narayanan [1,2], David Setton [3], Katherine E. Whitaker [4,2], Rachel Bezanson [3], Elia Cenci [5,6], Romeel Davé [7,8], Vincenzo R. D'Onofrio [9], Robert Feldmann [6], Jenny Greene [10], Mariska Kriek [11], Massimiliano Parente [1], Justin Spilker [9], Katherine A. Suess [12], Dariannette Valentín-Martínez [1], and Dhruv Zimmerman [1]

[1] *University of Florida Astronomy, 211 Bryant Space Science Center, Gainesville, FL, 32611, USA*
[2] *Cosmic Dawn Center (DAWN), Copenhagen, Denmark*
[3] *Department of Physics and Astronomy and PITT PACC, University of Pittsburgh, Pittsburgh, PA 15260, USA*
[4] *Department of Astronomy, University of Massachusetts, Amherst, MA 01003, USA*
[5] *Department of Astronomy, University of Geneva, Chemin Pegasi 51, Versoix CH-1290, Switzerland*
[6] *Department of Astrophysics, Universität Zürich, Winterthurerstrasse 190, Zurich CH-8057, Switzerland*
[7] *University of Edinburgh, Institute for Astronomy*
[8] *Department of Physics and Astronomy, University of the Western Cape, Bellville, Cape Town 7535, South Africa*
[9] *Department of Physics and Astronomy and George P. and Cynthia Woods Mitchell Institute for Fundamental Physics and Astronomy, Texas A&M University, 4242 TAMU, College Station, TX 77843-4242, USA*
[10] *Department of Astrophysical Sciences, Princeton University, 4 Ivy Lane, Princeton, NJ 08544, USA*
[11] *Leiden Observatory, Leiden University, P.O. Box 9513, 2300 RA Leiden, The Netherlands*
[12] *Department for Astrophysical & Planetary Science, University of Colorado, Boulder, CO 80309, USA*

ABSTRACT

Observations of quenched galaxies across cosmic time have revealed systems containing substantial molecular gas reservoirs, challenging the traditional picture of gas-poor, red and dead galaxies. Using the SIMBA cosmological simulation, we investigate three possible hypotheses for the origin of molecular gas-rich quenched systems: (i) quiescence is temporary and the galaxy will rejuvenate, (ii) molecular gas masses are overestimated due to an underestimated CO-to-H_2 conversion factor, or (iii) star formation is ongoing but heavily obscured by dust. Across $M_* > 3 \times 10^9 M_\odot$ galaxies from $z = 0 - 2$, we find that all three mechanisms are plausible. Many seemingly quiescent, molecular gas-rich galaxies host dust-obscured star formation, with visual optical depths increasing on average from $\tau_V \sim 0.5 - 2.3$ from $z = 0 - 2$. Assuming a Milky Way-like CO-to-H_2 conversion factor can overestimate molecular gas masses by a factor of $\sim$5 in non-star-forming galaxies, compared to $\sim$1.45 in star-forming galaxies. Temporary quiescence can also occur in gas-rich transitioning galaxies on timescales ranging from 100 Myr − 2 Gyr, although this is most prominent at high redshift and is relatively rare overall. Further work is needed to disentangle the relative contributions of these mechanisms across cosmic time.

Keywords: Molecular gas (1037) — Quenched galaxies (2016) — Star formation (1596)

1. INTRODUCTION

Observations of galaxies in the local universe find a persistent bimodality in galaxy populations (e.g. Noeske et al. 2007; Wuyts et al. 2011; Brammer et al. 2011; Muzzin et al. 2013; Jin et al. 2014). This dichotomy is defined by one population of star-forming galaxies that are blue in color with spiral morphology (Saintonge et al. 2012; Tacconi et al. 2018), and a second population, traditionally called quiescent or 'red and dead' galaxies, which have their star formation quenched and have typically early-type morphological structures (Blanton et al. 2003; McDermid et al. 2015). In the Local Universe, star-forming galaxies are observed to be gas-rich relative to their quiescent counterparts (Davis et al. 2012; Young et al. 2014).

Studies of massive galaxies at high-z confirm that the majority of quenched systems form their stars early on and in short bursts (Carnall et al. 2018; Belli et al. 2019; Merlin et al. 2019; Suess et al. 2021; Laporte et al. 2021; Tacchella et al. 2022). One such product of this rapid quenching are the so-called "post-starburst galaxies" (hereafter 'PSB' galaxies), which are thought to be the direct result of massive galaxies undergoing a strong burst of star formation that dramatically shuts down

within $\lesssim 1$ Gyr (Dressler & Gunn 1983; Zabludoff et al. 1996; Goto 2005, 2007; Yang et al. 2008; Kriek et al. 2010; Wild et al. 2020; French 2021). PSB galaxies are most common at Cosmic Noon, contributing to half of the total growth of quenched galaxies at $z \sim 2$ (Belli et al. 2019), though they are relatively rare in the local universe, representing only $\sim 20\%$ of transitioning galaxies at $z \sim 1.4$ and a negligible fraction at $z \sim 0$ (Tran et al. 2004; Whitaker et al. 2012; Wild et al. 2016; Lotz et al. 2021; Setton et al. 2023; Smercina et al. 2022; Park et al. 2024).

Since such galaxies are assumed to be shutting down their star formation and transitioning to being fully quenched, traditional star formation laws suggest that they should be relatively devoid of molecular gas (e.g. Kennicutt 1998; Schmidt 1959). In recent years, there has been a flurry of activity in observationally studying the cold gas reservoirs in PSB galaxies (Rowlands et al. 2015; French et al. 2015; Alatalo et al. 2016, 2017; Suess et al. 2022; Setton et al. 2025). Contrary to traditional expectations, such observations have revealed that PSB galaxies can retain significant reservoirs of CO-traced molecular (H_2) gas, with molecular gas fractions up to $\sim 20\%$ at $z < 1$, even after shutting down their star formation (Young et al. 2014; Suess et al. 2017; French et al. 2018b; Bezanson et al. 2022; Baron et al. 2022; Setton et al. 2025; Umehata et al. 2025). Interestingly, the molecular gas fraction in these galaxies is a strong function of the time elapsed since quenching (Suess et al. 2025). However, as noted by Bezanson et al. (2022), the inferred gas depletion timescales for such galaxies ($\sim$Gyr) is significantly longer than their observed quenching timescale ($\sim$100-200Myr). These findings indicate that the quenching of star formation in PSBs is not directly driven by gas exhaustion; instead suggesting that the molecular gas reservoirs are rendered inhospitable to star formation either through the heating or removal of ISM gas.

While quenching in such systems has been studied since Dressler & Gunn (1983), a clear picture of the processes driving its onset has yet to emerge. The most commonly proposed mechanisms include processes internal to galaxies (morphological quenching or AGN feedback; e.g., Martig et al. 2009; Baron et al. 2018; Calabrò et al. 2019) as well as environmental effects like ram-pressure stripping, galaxy mergers, and starvation (e.g., Blanton & Moustakas 2009; Snyder et al. 2011; Lotz et al. 2021; Spilker et al. 2022; D'Onofrio et al. 2025). However, the timescales associated with many of these mechanisms are not able to account for the rapid quenching observed at high redshift (Yesuf et al. 2014; French et al. 2018a; Veilleux et al. 2005; French 2021; Bezanson et al. 2022). These questions, along with the difficulty of explaining the large molecular gas abundances detected in such systems (e.g., Yesuf & Ho 2020; Cenci et al. 2025; Setton et al. 2025), pose a challenge for models of galaxy evolution.

Motivated by this, the goal of this paper is to holistically investigate the various proposed pathways that can result in recently quenched high-mass galaxies preserving their molecular gas with cosmological galaxy simulations. In particular, we investigate three potential physical scenarios for the existence of copious molecular gas reservoirs remaining in massive galaxies with seemingly low star-formation rates.

Our first hypothesis is that recently quenched massive galaxies, with observable levels of molecular gas, may simply be in a temporary period of dormancy, and are on a path to rejuvenation (Remus & Kimmig 2023; Kimmig et al. 2025). Multiple theoretical studies support this: Lotz et al. (2021) found that $\sim 23\%$ of massive quiescent galaxies undergo rejuvenation when tracked forward from $z = 3.4$ in the MAGNETICUM PATHFINDER simulation suite. Harrold et al. (2025) used a semi-analytic model to show that a typical massive and recently quenched galaxy at $z = 1$ has a $\sim 25\%$ chance of rejuvenating within 1 Gyr. Finally, Ángel Chandro-Gómez et al. (2025) used the new COLIBRE simulations to show that up to half of massive quenched galaxies could rejuvenate after initial quenching. Observational studies independently support this hypothesis, such as the work by Ellison et al. (2025) in which FAST 21 cm observations of 68 PSB galaxies were used to show that at low redshift these systems can contain HI gas fractions up to 30%. The presence of substantial atomic gas reservoirs observed in these rapidly quenched galaxies suggests that such PSB-like systems do not quench through the wholesale removal of their gas, and therefore remain viable candidates for future rejuvenation.

The remaining two hypotheses that we investigate deal with observational effects that could result in the inference of molecular gas present in seemingly quenched galaxies. Possible solutions could be that the molecular gas is not as abundant as it seems to be (Hypothesis 2), or that the galaxy is not actually as quenched as it appears (Hypothesis 3). In particular, our second hypothesis investigates whether molecular gas mass estimates are impacted by potentially varying CO-to-H_2 conversion factors (Narayanan et al. 2012; Bolatto et al. 2013), and our third hypothesis asks whether dust attenuation mimics colors compatible with selection as a quenched galaxy (Akins et al. 2022; Baron et al. 2023; Davis et al. 2019; Cenci et al. 2025). The latter hypothesis is also supported by evidence that typical massive

quenched galaxies at cosmic noon ($z \sim 2.5$) are significantly more reddened than those in the local universe, with dust attenuation falling from $A_V \sim 0.5$ at $z = 2.5$ to near zero at present times (Siegel et al. 2024).

This paper is organized as follows. In §2, we describe the numerical methods that we employ, starting with the simulation we use (§2.1), the dust model it implements (§2.1.1), and the updates to its black hole feedback model (§2.1.2). In §2.2, we discuss how we track galaxies across different snapshots using progenitor and descendant tracking. In §2.3 we define our galaxy selection criteria, first by defining our method for classifying quenched/transitioning galaxies (§2.3.1), followed by an explanation of the photometric selection criteria we use to investigate observational systematics (§2.3.2). In §3, we present the results of our analysis: specifically, in §3.1 we examine temporary quiescence, in §3.2 the impact of $\alpha_{\rm CO}$, and finally in §3.3 we investigate the impact of dust obscuration. Next, in §4, we discuss how our simulation and methodology compares to other analogous numerical studies. Finally, in §5 we conclude by summarizing our results, their implications, and avenues for future work on this topic.

2. METHODS

2.1. *Cosmological Simulations*

We employ the SIMBA galaxy formation simulation (Davé et al. 2019), which is a modern cosmological simulation that includes models for star formation, its associated feedback, black hole growth/feedback, and interstellar dust. Specifically, we employ the fiducial (25/h Mpc)^3 box with 2×512^3 particles, resulting in a baryon mass resolution of $M_{\rm b} \approx 2 \times 10^6 M_\odot$.

The SIMBA simulation employs the meshless finite mass (MFM) hydrodynamic solver within the GIZMO codebase (Hopkins 2015, 2017). SIMBA includes a subresolution prescription for star formation and feedback. Here, star formation occurs stochastically in H_2 gas, where the molecular content is determined using the Krumholz, McKee, & Tumlinson (2009) algorithm, which calculates the fraction of gas in molecular hydrogen ($f_{\rm H_2} \equiv M_{\rm H_2}/M_{\rm gas}$) as a function of metallicity and column density (Davé et al. 2016). More information about this algorithm can be found in Krumholz & Gnedin (2011).

Star formation follows a volumetric Schmidt (1959) law (hereafter SFR $\equiv \dot{M}_*$ = Star Formation Rate):

$$\mathrm{SFR} \equiv \epsilon_* \left(\frac{\rho_{\rm gas} \times f_{\rm H_2}}{t_{\rm ff}} \right) \propto \rho_{\rm gas}^{3/2} \qquad (1)$$

where $\epsilon_* = 0.02$ is the fixed efficiency of star-formation per free-fall time, and $t_{\rm ff}$ is the free-fall time-scale ($t_{\rm ff} = \sqrt{3\pi/(32 G \rho_{\rm gas})} \propto \rho_{\rm gas}^{-1/2}$). By construction, the star-formation rate is directly dependent on the density of its gas ($\rho_{\rm gas}$), and its molecular gas fraction ($f_{\rm H_2}$). In their formalism, they also require a minimum density for star formation of $n_H \geq 0.13\,{\rm cm}^{-3}$, defining gas with densities above this as 'ISM gas' (Davé et al. 2016).

2.1.1. *Dust Model*

SIMBA includes a model for dust physics that is able to capture the formation and evolution of cosmic dust. Due to the inability to resolve gas drag in our simulation, along with the very short time scales associated with it, the model has dust passively follow the flow of gas particles. The modeled dust grains have a single fixed radius of $a = 0.1$ μm, and active dust cooling is ignored (Davé et al. 2019).

Following the prescription of Dwek (1998), cosmic dust is produced by metal condensation in the ejecta of supernovae (SNe) and Asymptotic Giant Branch (AGB) stars. After being produced, the model allows dust to grow in mass by accreting gas-phase metals; in which dust particles collide with gaseous metals, causing the metals to stick to the dust grains and allowing their mass to grow. In addition, thermal sputtering is implemented so that dust grains can be eroded by thermally excited gas (Davé et al. 2019). Finally, since the simulation cannot resolve individual supernovae (SNe) shocks, an additional dust destruction mechanism by SNe shocks is included, following the prescription from McKinnon et al. (2016). The dust model, fully detailed in Li et al. (2019), shows good agreement with observational constraints on dust abundance, especially its redshift evolution (Parente 2025).

2.1.2. *Black Hole Model*

SIMBA includes on-the-fly black hole growth and AGN feedback, fully described in Davé et al. (2019); here we summarize the features salient to this work. Black holes grow via a two-mode accretion model: torque-limited accretion from cold gas ($T < 10^5$ K), following Hopkins & Quataert (2011) and Anglés-Alcázar et al. (2017), and Bondi (1952) accretion from hot gas ($T > 10^5$ K). Feedback is implemented kinetically as bipolar outflows, with the mode set by the Eddington ratio of the galaxy's most massive black hole. At $f_{\rm Edd} > 0.2$, AGN drive multi-phase 'radiative mode' winds, which have only a modest effect on galaxy populations (Davé et al. 2020). When $f_{\rm Edd} < 0.2$ and $M_{\rm BH} > 10^{7.5} M_\odot$, feedback transitions to 'jet mode', driving hot collimated outflows whose velocity increases as $f_{\rm Edd}$ drops, up to an additional 7000 km s^{-1} at $f_{\rm Edd} \leq 0.02$. Finally, when $f_{\rm Edd} < 0.02$ and $f_{\rm gas} \equiv M_{\rm gas}/M_* < 0.2$, X-ray heating of the ISM is

included, imparting a radial outward kick and temperature increase.

The jet mode is primarily responsible for quenching and maintaining the massive quenched population in SIMBA , heating the circumgalactic gas and shutting off the inflow of fresh gas (Davé et al. 2019; Hardcastle et al. 2007), while the X-ray mode supplies the additional energy needed to quench star formation in massive galaxies.

2.2. *Progenitor/Descendant Tracking*

After the execution of the SIMBA simulation, we employ CAESAR (Thompson 2014), a YT-based package (Turk et al. 2011), to identify dark-matter halos and galaxies using a 6D friends-of-friends algorithm. For each snapshot, CAESAR outputs a cross-matched halo and galaxy HDF5 catalog, with an abundance of precomputed properties for each (Davé et al. 2019), as well as the particle data used to calculate them. In order to track a single galaxy through time, we must link galaxies across multiple snapshots: here we describe this progenitor and descendant tracking of galaxies through cosmic time.

In order to track a single galaxy backwards through time (to higher z) we must use progenitor tracking. Since any one galaxy would have had many ancestral galaxies that merged to produce it, tracking galaxies backwards in time requires following *all* galaxies that share common star particles with it at any point in the past. In practice, we identify a galaxy of interest at $z = 0$, and then increment through successive higher redshift snapshots, searching for all galaxies that share at least 10% star particles in common with our galaxy of interest, all of which will be considered its progenitors. Since all such galaxies will eventually contribute to our target galaxy at $z = 0$, we must sum up *all* of their properties to effectively compare across snapshots. Conceptually, this is essentially calculating the merger tree for any target galaxy.

While this method works for moving backward in time, if we wanted to track a galaxy forward in time (to lower z) we would instead be tracking its descendants. This becomes necessary, for example, when we want to see at a given redshift if a galaxy will rejuvenate as time increases. As discussed in the literature (e.g. Torrey et al. 2015), this process is fundamentally different from progenitor tracking due to the nature of mergers. While tracking a galaxy backwards in time using a merger tree requires calculating the sum of all the progenitors, in our formalism tracking it forward in time requires only the most massive parent node to be tracked up the tree. This is because while tracking galaxies forward in time a significant fraction of the population can be 'lost' via merger events, no such loss occurs when tracking backward in time (Torrey et al. 2015).

2.3. *Galaxy Selection Criteria*

We focus our study on massive quenched galaxies comparable to current theoretical work (Davis et al. 2019; Setton et al. 2025) and observational surveys (e.g. Rowlands et al. 2015; French et al. 2015, 2018a,b; Suess et al. 2022; Bezanson et al. 2022; Baron et al. 2023; French et al. 2023; Spilker et al. 2025), and therefore impose a minimum mass requirement. Following the methodology of Cenci et al. (2025), in order to compare best with recent observations such as Suess et al. (2022) we restrict our analysis to galaxies with stellar masses $M_* > 3 \times 10^9 M_\odot$, producing an initial sample of 395 galaxies at $z = 0$ (245 at $z = 1$, 110 at $z = 2$, and 60 at $z = 3$). All galaxies satisfying this mass cut are shown on a plot of stellar mass vs SFR in Fig. 1 for $z = 0, 1, 2$.

2.3.1. *Star Formation Classification*

Following Rodríguez Montero et al. (2019); Tacchella et al. (2022), we employ a combination of the specific star formation rate (sSFR $\equiv$ SFR/M$_*$) and the age of the Universe at the time of galaxy identification (t$_H \equiv 1$/H(z)) to decide whether a galaxy is star-forming (sSFR $\geq 0.7/t_H$), fully quenched (sSFR $\leq 0.3/t_H$), or intermediate/transitioning between the two:

$$\text{Star Forming}: \quad \text{sSFR} \times t_H \geq 0.7 \tag{2}$$

$$\text{Transitioning}: \quad 0.7 > \text{sSFR} \times t_H > 0.3 \tag{3}$$

$$\text{Quenched}: \quad \text{sSFR} \times t_H \leq 0.3 \tag{4}$$

Specifically, since 1/sSFR gives the timescale for a galaxy to double its stellar mass, as described in Tacchella et al. (2022), comparing it to t$_H$ gives an estimate of the number of times the stellar mass has doubled within the age of the universe (assuming a constant sSFR). To put this into context, the Milky Way would have sSFR $\times$ t$_H \sim 0.4$ (Licquia & Newman 2015), thus would be defined as 'transitioning', have a stellar mass-growth timescale of 2.5t$_H$, and at its current level of star-formation would have formed 40% of its existing stellar mass over a Hubble time.

In Fig. 1, we show the regime we would define as 'star-forming' according to Eq. 2 with a blue background, 'transitioning' (Eq. 3) in yellow, and 'quenched' (Eq. 4) in red. While a quenching threshold of sSFR $\times$ t$_H \leq 0.2$ is more common (Tacchella et al. 2015; Pacifici et al. 2016; Whitaker & Bezanson 2026), we adopt the slightly more inclusive value of 0.3 (following, e.g., Franx et al. 2008; Williams et al. 2010; Szomoru et al. 2013; Lotz

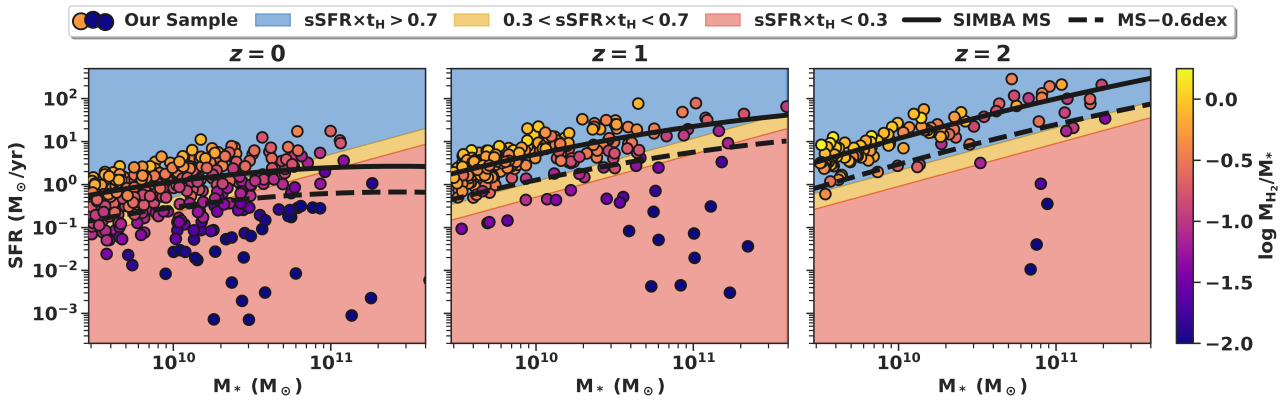


Figure 1. Full galaxy sample shown along with our adopted selection criteria, as well as with a comparison to alternate methods. Each point represents a $M_* > 3 \times 10^9 M_\odot$ galaxy in our SIMBA simulation, with a color corresponding to the log ratio of total molecular (H_2) to stellar mass. The blue shaded region highlights where we define galaxies to be 'star forming' (Eq. 2), while the yellow region below that corresponds to 'transitioning' (Eq. 3), and the red region below that for fully 'quenched' (Eq. 4). For comparison, the star forming main sequence (SFMS) for SIMBA is shown as solid black line (derived by fitting our data to the functional form of Whitaker et al. 2014, Eq. B1), while the dashed black line shows where galaxies have SFRs that lie 0.6 dex below the SFMS. While in general our definition of quenched galaxies (Eq. 4) captures approximately the same galaxy population as are 1 dex below the SFMS, we see that at $z = 0$ the two definitions differ most at the high-mass end. A full comparison of these methodological choices is explored in Appendix B.1

et al. 2019), as our aim is to broadly capture low star-forming systems rather than isolate the most strictly quenched galaxies.

Among our initial sample of $M_* > 3\times10^9 M_\odot$ galaxies, we find that at $z = 0$ that 249 (63%) are "star-forming", 54 (14%) are "transitioning", and 92 (23%) are fully "quenched". This is consistent with the numerical results from Donnari et al. (2019), which used rest-frame UVJ photometric colors to identify star-forming galaxies in the IllustrisTNG simulations, predicting that 71% of $M_* > 10^9 M_\odot$ galaxies will be star-forming. Moving to higher redshift, we find that at $z = 1$ the number of "star-forming"/"transitioning"/"quenched" galaxies decreases to 213/7/25 (87%/3%/10%), at $z = 2$ this becomes 99/6/5 (90%/5%/5%), and at $z = 3$ we find 59/0/1 (98%/0%/2%). While the lack of high-mass galaxies at high-z is what causes the numbers to decrease so rapidly, we find in contrast that the fraction of star-forming galaxies increases with redshift. This is consistent with a number of observational studies, such as Weaver et al. (2023), who studied galaxies from $z = 7.5 \rightarrow 2$ from the COSMOS2020 observational catalog using their rest-frame near-ultraviolet (NUV), r, and j band colors, and found that at $z \geq 2$, around 90% of galaxies will be star-forming.

An alternative method for classifying star-forming galaxies is to measure their offset from the Star-Forming Main Sequence (SFMS; e.g. Noeske et al. 2007; Whitaker et al. 2012, 2014; Speagle et al. 2014), the well-established relation between stellar mass (M_*) vs star-formation rate (SFR). Since galaxies become increasingly quiescent as they move below the SFMS, systems lying more than 0.6 dex beneath the relation are considered 'transitoning', while those more than 0.9 dex below are fully 'quenched' (Donnari et al. 2019; Bluck et al. 2020; Whitaker & Bezanson 2026).

To see how this selection method compares to our own, we show in Fig. 1 the SFMS for SIMBA a solid black line, calculated by fitting our data at each redshift to the functional form of Whitaker et al. (2012) (via Eq. B1), with details provided in Appendix B.1, and an associated dashed black line showing where galaxies are 0.6 dex below this SFMS. In our formalism (Eq. 2-4), this dashed line can be compared to the top of our yellow region, which we use to show where our transitioning galaxies lie (Eq. 3). Doing so shows that both definitions capture a similar population of non star-forming galaxies (i.e. transitioning or quenched), with the worst correspondence occurring at low-z and high mass. This arises from the known fact that the SFMS slope flattens at the massive end at low redshift (Abramson et al. 2014), possibly due to the combination of an older bulge and younger disk (Whitaker et al. 2015).

In Appendix B.1 we describe in detail how we calculated the SFMS for SIMBA, how it is traditionally used to categorize star-forming galaxies, and how this definition differs from the $\mathrm{sSFR}\times\mathrm{t_H}$ definition we used in this study. In summary, given these differences, we choose to avoid using a SFMS-based definition for quenching, partly because the redshift evolution of the SFMS differs between simulations and observations (Bluck et al. 2023), and also as shown in Appendix B.1, our sSFR-

based method of identifying 'low star-forming' systems produces a population of systems much more gas-rich than if we used the SFMS method. Therefore, we adopt our sSFR-based definition of quenching, given in Eq. 2-4, as it is non-dimensional, invariant across redshift, and yields a more gas-rich sample.

2.3.2. *UBV-Selection*

While for the majority of the analysis we want to use a physical definition of quenching, as described in the previous section (§2.3.1), there will be a point where we will investigate potential observational systematics in selecting quenched systems. Specifically, this becomes important while investigating our third hypothesis (§3.3), in which we ask whether dust could obscure ongoing star formation in seemingly quenched systems, creating false signatures of quenching in otherwise star-forming, molecular gas rich galaxies. Because of the nature of this hypothesis, we naturally want to select galaxies in as faithful to an observational manner as possible.

To derive mock colors for our simulated galaxies, we must first create synthetic spectra. To generate realistic mock spectral energy distributions (SEDs) for our sample of galaxies, we post-process our simulated snapshots using the dust radiative transfer code POWDERDAY (https://github.com/powderday-rt/powderday). First introduced in Narayanan et al. (2021), POWDERDAY uses FSPS for stellar population synthesis models (Conroy et al. 2009, 2010; Conroy & Gunn 2010), HYPERION for radiative transfer (Robitaille 2011), and YT to interface between varying software packages (Turk et al. 2011).

When running POWDERDAY to produce mock SEDs, we smooth the particle data onto an octree to setup the model for radiative transfer. Next, we employ FSPS to generate a simple stellar population (SSP) for each star particle. For consistency with SIMBA, we use a Chabrier initial mass function (IMF) (Davé et al. 2019). Combined with MIST isochrones (Choi et al. 2016; Dotter 2016) and a MILES stellar spectral library (Sánchez-Blázquez et al. 2006) as our fiducial SPS parameters, we then run FSPS to create a dust-free stellar SED. Given the initial stellar SED from FSPS and the grid from YT, HYPERION is then employed to run 3D radiative transfer via a Monte Carlo algorithm to produce the final SED (Robitaille 2011). Finally, the resulting SED is extracted by assuming the largest aperture size available to the model.

To construct our photometric selection criteria, we follow the Kriek et al. (2010) method, also used by Suess et al. (2022), which uses synthetic medium-band rest-frame filters (U_m, B_m, and V_m) to define "post-starburst galaxies" (hereafter PSBs) as

$$\underline{\text{UBV-Selected}}\ (\text{"PSB-like"})\ \text{Galaxies:}$$
$$U_m - B_m > 0.975 \quad \& \quad -0.25 < B_m - V_m < 0.45 \tag{5}$$

According to Suess et al. (2022), the $U_m - B_m$ color is able to separate PSBs from unobscured star-forming galaxies by quantifying the strength of the Balmer break, while the $B_m - V_m$ color is able to separate PSBs from dusty star-forming galaxies and older quiescent galaxies by quantifying the slope of the spectra redwards of the break. Collectively, these photometric cuts are meant to identify relatively dust-free galaxies that recently quenched after a large starburst. Since we are using this method to identify our sample of galaxies in §3.3, it is informative to check how our resulting sample differs from the sample produced by Suess et al. (2022), which is done in Appendix B.2.

Applying this photometric cut to our initial sample of $M_* > 3{\times}10^9 M_\odot$ galaxies results in a sample of 21 (5.3%) UBV-selected galaxies at $z = 0$. In agreement with the findings from Belli et al. (2019) that PSB galaxies are most common at Cosmic Noon, we find that the highest fraction of UBV-selected galaxies in our sample occurs at $z = 2$, dropping off both at higher and lower redshifts than this. Specifically, at $z = 1$ we find 48 galaxies (20%) in our sample are UBV-selected, at $z = 2$ we find 30 (27%), while at $z = 3$ this rapidly drops to only 10 galaxies (17%) which satisfy our UBV-selection.

Applying this selection criterion to our sample of galaxies at $z = 0.5$ produces the population colored red in the top plot of Fig. 2. The left-hand panel shows all of our galaxies in UBV-space as individual points, while the red colored dots are those galaxies that satisfy the 'PSB-like' UBV-selection criteria (Eq. 5). The right-hand plot of Fig. 2 shows the same sample using alternative definitions; namely the 4000Å break (D_n4000) and Lick index ($H\delta_A$). The 4000Å break, commonly called the D_n4000 index, is used largely to determine a galaxies' current state of star formation (Poggianti & Barbaro 1997), and is defined as the ratio between the average flux density (in erg $s^{-1}cm^{-2}Hz^{-1}$) between 4000-4100Å and 3850-3950Å.

In contrast, $H\delta_A$ is a Lick index developed as a standardized measure of the equivalent width of the Balmer $H\delta$ absorption line (Worthey & Ottaviani 1997), which is strongest for galaxies with stellar populations dominated by A-type stars, and is usually interpreted as evidence of a burst of star formation that ended 0.5-1.5 Gyr prior to observation. To calculate this, a pseudo-continuum is defined by calculating the average flux density bluewards of the line (4017Å-4057Å) and redwards of the line (4153Å-4193Å), fitting a straight line

between both, then using that to integrate over the absorption line (defined between wavelengths 4083.5Å and 4122.25Å). The subscript "A" is used to define a wider bandpass, around 40Å, which is more suited for measuring absorption in A-star dominated systems with intrinsically broader absorption (Worthey & Ottaviani 1997).

In the bottom panel of Fig. 2, we plot all UBV-selected galaxies at $z = 0.5$, colored by their logarithmic dust mass, with their stellar mass on the x-axis, and their molecular (H_2) gas mass on the y-axis. For context, we plot as 2D KDE distributions the associated values for non UBV-selected systems, colored by whether they are star forming (Eq. 2; blue), transitioning (Eq. 3; yellow), or quenched (Eq. 4; red). From this plot, we can see that while the majority of UBV-selected galaxies have masses comparable to typical star-forming galaxies, the most dust-rich systems instead have higher molecular masses, comparable to typical quenched galaxies.

3. RESULTS

To investigate the mechanisms that could give rise to observations of massive quenched galaxies harboring significant molecular gas reservoirs, we divide our theories into three hypotheses, originally discussed in the introduction (§1), to individually study their relative contributions across cosmic time. We now discuss our results in the context of these hypotheses in turn.

3.1. *Hypothesis A: Temporary Quiescence*

Our first line of investigation is to study whether or not massive galaxies that are quenching (or quenched), with significant reservoirs of molecular gas, are simply in a dormant state and not permanently quiescent; i.e., are these galaxies destined for rejuvenation (Remus & Kimmig 2023; Kimmig et al. 2025)? Indeed, as discussed in the introduction (§1), many theoretical and observational studies have concluded that rejuvenation can play an important role in galaxy evolution (Lotz et al. 2021; Remus & Kimmig 2023; Kimmig et al. 2025; Harrold et al. 2025; Ángel Chandro-Gómez et al. 2025; Cenci et al. 2025; Setton et al. 2025).

To define a rejuvenation event, we loosely follow the formalism of Rodríguez Montero et al. (2019): here, a galaxy is defined to have rejuvenated if "after being quenched for a sufficient time, it has its sSFR return back over the star-forming cut". Specifically, Rodríguez Montero et al. (2019) defines a rejuvenating galaxy as one that after its sSFR falls below their quenching threshold of $0.2/t_H$, it remains below t_H^{-1} for at least $0.2t_H$ before having its sSFR rise back above t_H^{-1}. Applying this to our sample, we instead define a galaxy to be a candidate for rejuvenation only if it has

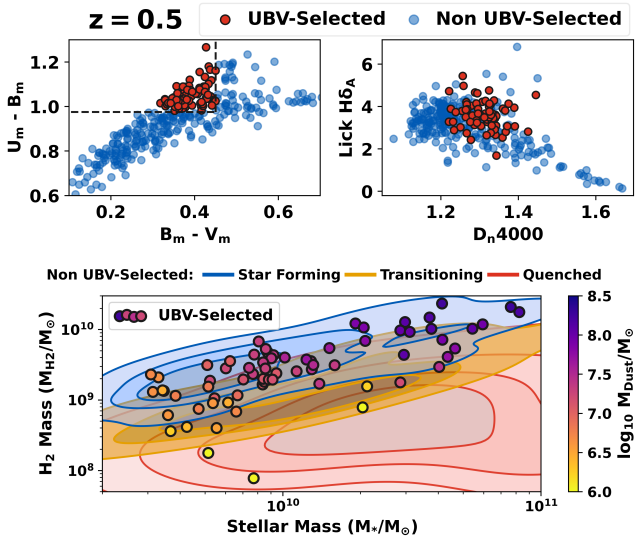


Figure 2. (Top) The distribution of our SIMBA galaxies at $z = 0.5$ in UBV space (left), and in a plot of D_n4000 vs $H\delta_A$ (right). The red-colored points are those that satisfy the PSB-like UBV selection (Eq. 5) from Suess et al. (2022), defined to identify relatively dust-free galaxies that recently quenched after a large starburst. The left-hand plot shows the galaxies in UBV-space, defined by the medium-band rest-frame filters (U_m, B_m, and V_m), designed to target the Balmer break and slope of the spectrum redward of the break (Suess et al. 2022). Right-hand plot shows the galaxies lick $H\delta_A$ index (i.e. $H\delta$ EW; which traces recent star formation) as a function of the 4000Å break index (which probes the age of the stellar population), such that age increases toward the lower right. **(Bottom) UBV-selected systems have masses comparable to typical star-forming galaxies.** All UBV-selected galaxies at $z = 0.5$ are shown as dots, colored by their logarithmic dust mass, with their stellar mass on the x-axis and their molecular gas mass on the y-axis. For context, we plot as 2D KDE distributions the associated values for non UBV-selected systems, divided by whether they are star forming (Eq. 2; blue), transitioning (Eq. 3; yellow), or quenched (Eq. 4; red).

$M_* > 3\times10^9 M_\odot$, and is either transitioning or quenched (Eq. 3/4) for more than one snapshot.

We then say that such a galaxy will have rejuvenated if it eventually rises back above the star-forming threshold (Eq. 2) for multiple snapshots, and we say it has quenched if it falls below our quenched threshold for more than five consecutive snapshots, or if if it reaches $z = 0$ without rejuventing. While the exact time between snapshots depends on redshift, they are evenly spread out with respect to the logarithmic scale factor ($\log a$), where the scale factor is calculated as a function of redshift as $a \equiv 1/(1+z)$. In contrast to Rodríguez Montero et al. (2019), we soften the requirement needed for the galaxy to become eligible for rejuvenation, as our goal here is not to focus exclusively on strongly quenched

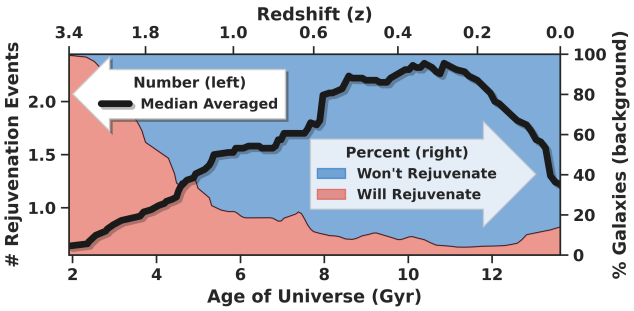


Figure 3. While the median number of rejuvenation events tends to increase toward present day, the fraction of $M_* > 3{\times}10^9 M_\odot$ galaxies with sSFR$\times$t$_H$ < 0.7 that will rejuvenate instead decreases over the same redshift range. The number of rejuvenation events at each snapshot is shown as a black line (left y-axis). Here, we see low values at high-z, due to the rarity of high-mass transitioning and quenched systems at these epochs, as described in §2.3/2.3.1. Additionally, we see another turnover at low-z, occurring around $z \sim 0.4$ ($t_H \sim 10$Gyr); this arises because galaxies identified within the last few Gyr of cosmic time simply have not had enough time to undergo the $\sim$ 2Gyr rejuvenation process. In contrast, the fraction of our massive transitioning or quenched galaxies that will rejuvenate, indicated by the red region (right y-axis) is highest at high-z, and decreases monotonically towards $z = 0$. The reason for this trend is that rejuvenation is primarily driven by galaxy interactions, which in this redshift/mass range are most common around $z \sim 3$, with decreasing rates towards lower z.

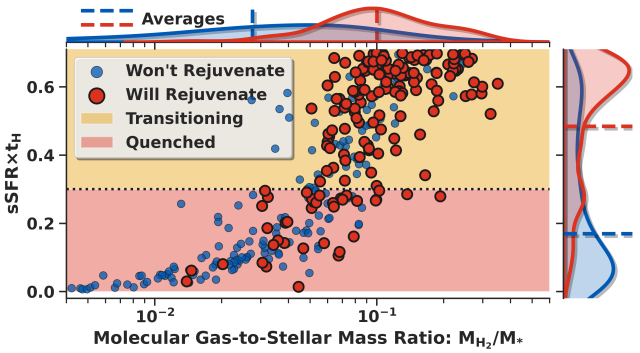


Figure 4. Rejuvenating galaxies are significantly more star-forming and gas-rich than their non-rejuvenating counterparts for $z = 0 - 3.5$. Every point represents a $M_* > 3 \times 10^9 M_\odot$ galaxy, either transitioning or quenched (Eq. 3/4), colored red if it will rejuvenate and blue if not, with its molecular gas-to-stellar mass ratio shown on the x-axis, and its associated value of sSFR$\times$t$_H$ on the y-axis. On the top/right sides of the plot we also show the marginal distributions for each population as a KDE plot, with the stellar mass weighted averages shown as dotted lines. We see from this that the majority of rejuvenating galaxies have $M_{H_2}/M_* > 0.1$ (solid black line), implying they are gas-rich, and are predominantly 'transitioning' (yellow region; Eq. 3), while those that will not rejuvenate are primarily quenched (red region; Eq. 4)

galaxies, but rather to broadly quantify the likelihood of rejuvenation in any low star-forming and high-mass galaxy.

The results of this analysis are shown in Fig. 3, where for each snapshot we show the median number of rejuvenation events (left), and the percent of galaxies that will (red) and won't (blue) rejuvenate (right). The left-hand y-axis shows as a black line the median averaged number of rejuvenation events that occur at each snapshot, where at each snapshot we take a median of the values within a moving window centered on that snapshot in order to smooth the data. In contrast, the right-hand y-axis shows the percent of our tracked galaxies at each snapshot that eventually will (red region) and won't (blue region) rejuvenate when tracked forward in time. Similar to the black line, these regions have been smoothed using a 1D Gaussian ($\sigma = 2$) filter from SCIPY.NDIMAGE[1], which replaces points with a weighted average of nearby points via a Gaussian kernel.

Examining Fig. 3, we see that while rejuvenation can be an important effect at high redshift, it reduces in relative likelihood at low redshift (as also found in Szpila et al. 2025). To expand on this, we see that while at high redshift the occurrence of rejuvenations is the highest, the sample size is also the smallest due to the lack of massive galaxies at high-z (as discussed in 2.3). In contrast, as redshift decreases, the number of $M_* > 3 \times 10^9 M_\odot$ transitioning/quenched (Eq. 3/4) galaxies that will rejuvenate increases towards a maximum value around $z \sim 0.4$, then again falls towards the present day ($z = 0$). The reason for this trend is two-fold. First, as will be shown later in this section, rejuvenation is primarily driven by galaxy interactions like mergers, which are most common for massive galaxies at $z \sim 3$ (Conselice 2007). In addition to the rarity of galaxy interactions capable of reigniting star formation in the local universe, the drop off at $z < 0.4$ could also be explained by the $\sim$Gyr timescales needed to reignite star-formation, so this turnover can also be thought of as an artifact arising from the lack of time needed to rejuvenate in the early universe. In other words, while such galaxies may still rejuvenate in the future, not enough time has passed for them to have rejuvenated by the present day.

Given the results of Fig. 3, it becomes instructive to ask what physical differences exist between those galaxies in our sample that rejuvenated or not. This is accom-

[1] https://docs.scipy.org/doc/scipy/reference/generated/scipy.ndimage.gaussian_filter1d.html

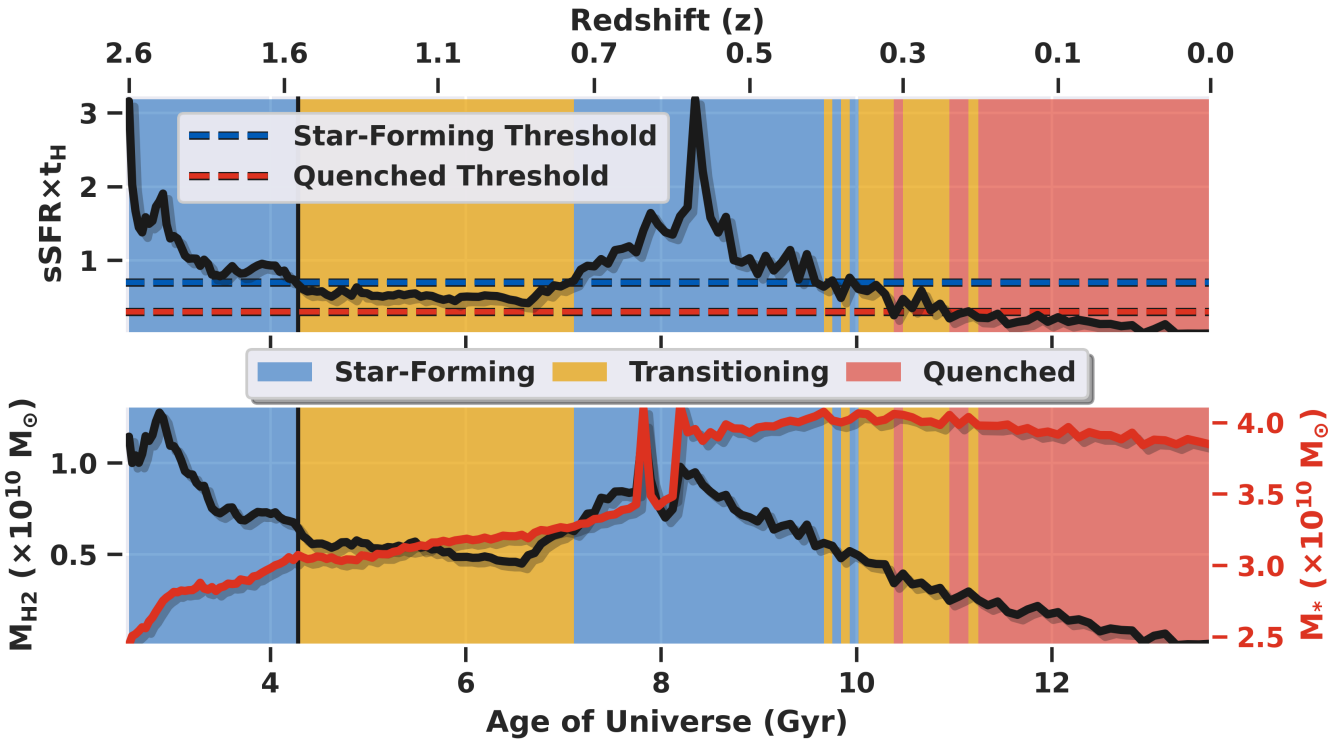


Figure 5. Example of a rejuvenating galaxy, selected at $z \approx 1.5$ (vertical black line; $t_H \sim 4.3$ Gyr), based on it satisfying both our conditions; (a) massive $M_* > 3 \times 10^9 M_\odot$ and (b) sSFR $\times$ $t_H < 0.7$ (transitioning or quenched), with the background color set to the star-forming classification of the galaxy based on Eq. 2-4. While the top panel shows the evolution of sSFR $\times$ t_H, the bottom panel shows the corresponding evolution of molecular gas mass (left/black) and stellar mass (right/red), both of which show a gradual evolution at high redshift, followed by a dramatic increase at around $z \approx 0.6$ driven by a major merging event. The drop-off after this and subsequent rise show that the merging galaxy initially passes through our main galaxy, but, now bound within its potential well, later falls back and ultimately merges with it. This scenario was confirmed in Appendix A via density projection plots of the galaxy at different stages in its evolution.

plished in Fig. 4, in which we include all galaxies from Fig. 3 on a plot of molecular gas-to-stellar mass fraction vs sSFR $\times$ t_H, for all snapshots from $z = 0 - 3.5$, colored only by whether they will (red) or won't (blue) rejuvenate. On the top/right sides of Fig. 4 we show the marginal distributions for each population as a KDE plot[2], calculated using the python-based MATPLOTLIB extension called SEABORN (Hunter 2007; Waskom 2021), with the stellar-mass weighted averages shown as dotted lines.

Examining the distributions in Fig. 4 along the x-axis, we see immediately that the galaxies that will rejuvenate are much more molecular gas-rich relative to those that won't, with $\sim$ 50% of rejuvenating galaxies having $M_{H_2}/M_* > 0.1$ (12% of non-rejuvenating systems satisfy this), while $\sim$ 90% of rejuvenating galaxies have $M_{H_2}/M_* > 0.05$ (in contrast to 40% of non-rejuvenating systems), consistent with observational studies of gas-rich quenched galaxies (e.g. French et al. 2015; Rowlands et al. 2015).

Examining the marginal distributions from Fig. 4 along the y-axis shows that rejuvenating galaxies are significantly more star forming than their non-rejuvenating counterparts for $z = 0 - 3.5$. The background color of the plot is shaded to represent their star-formation classification according to §2.3.1, where the yellow background corresponds to 'transitioning' (Eq. 3), while the red background is 'quenched' (Eq. 4). We see that galaxies that won't rejuvenate have values of sSFR $\times$ t_H skewed towards the smallest values, with an average value that would fall in our 'quenched' category (Eq. 4), implying that these systems are fully quiescent, while those that will rejuvenate have the opposite trend, with an average value in our 'transitioning' regime. Specifically, we find that while $\sim$ 80% of rejuvenating systems will reside in the transitioning regime (Eq. 3), only

[2] A kernel density estimate (KDE) plot is a method for visualizing the distributions in a dataset, analogous to a histogram, with the important difference that instead of discrete bins observations are smoothed with a Gaussian kernel, producing a continuous density estimate such that the area under the curve is unity.

around 35% of non-rejuvenating systems will satisfy this (65% fully quenched). Taken as a whole, Fig. 4 shows that the galaxies that will rejuvenate are both (a) rich in molecular gas (relative to stellar mass) and (b) are not yet fully quenched.

To probe deeper, we show the individual star formation history (SFH) for an example rejuvenating galaxy in Fig. 5. This galaxy was selected at $z \approx 1.5$ (vertical black line; $t_H \sim 4.3$ Gyr), based on it satisfying both our conditions for having $M_* > 3 \times 10^9 M_\odot$ and being transitioning (Eq. 3), with the background color set to the star-forming classification of the galaxy based on Eq. 2-4. The galaxy was tracked forward in time using descendant tracking, and backward to $t_H \sim 2.6$ Gyr using progenitor tracking (see §2.2 for details). The bottom panel shows the evolution of H_2 mass (left/black) and stellar mass (right/red), showing that this galaxy has $M_* > 3 \times 10^9 M_\odot$ for all points in time.

The top panel shows the corresponding evolution of sSFR $\times$ t_H as a solid black line, showing how after initially being identified as transitioning at $t_H = 4.3$Gyr, we say the galaxy has rejuvenated approximately 2.8Gyr later at $t_H = 7.1$Gyr. This rejuvenation event is followed by a rapid increase in SFR, followed by a complete quenching event, which occurs in our formalism at $t_H = 11.2$ Gyr. Furthermore, this rejuvenation event in its star formation is seen to follow a dramatic increase in both the galaxy's molecular gas content and stellar mass at around 8 Gyr (bottom row of Fig. 5), indicating a major gas-rich merging event occurring here. Confirmation of this scenario was achieved by examining the projection plots of our target galaxy over time, shown in Appendix A, in which we can visually observe the companion galaxy passing through our target system and eventually merging with it. More details about this interaction and the associated projection plots are shown in Appendix A.

In summary, by examining the example rejuvenating galaxy in Fig. 5, we learned that rejuvenation events can be triggered by a gas-rich major merging event. In Fig. 4, we combined our sample of high-mass and low star-forming galaxies over all $z = 0 - 3.5$ to show that those galaxies that will rejuvenate are more gas rich and have significantly higher levels of star formation than those that do not rejuvenate. With Fig. 3 we analyzed the redshift dependence associated with rejuvenation, and showed that the highest probability of rejuvenation occurs at high redshift. Despite having the lowest sample size of galaxies that fit our selection criteria at high-z due to the effects of our high-mass cut, as discussed in §2.3, the abundance of major mergers at high-z is most likely what drives the high probability of rejuvenation here. In contrast, while the largest sample of massive galaxies are found at low redshift, the probability of rejuvenation here is also the smallest. While such galaxies may still rejuvenate in the future, the salient point is that they have not yet had time to rejuvenate by $z = 0$.

Putting it all together paints a picture in which among the transitioning or quenched massive galaxies, those that will rejuvenate are those that are relatively more molecular (H_2) gas rich and have not yet fully quenched. While these findings could potentially explain why galaxies with persistent molecular gas reservoirs could appear to have anomalously low SFRs, such as those from Suess et al. (2022) ($0.5 < z \leq 0.9$), it does not resolve the question of why their molecular gas seems to disappear on extraordinarily fast (~ 150 Myr) timescales (Setton et al. 2025).

3.2. *Hypothesis B: Incorrect Alpha-CO*

Our second hypothesis explores whether an incorrectly assumed value of the CO-to-H_2 conversion factor (α_{CO}) could be the root cause of the seemingly abundant molecular gas reservoirs observed in massive quenched galaxies. Since H_2 resides primarily in cool giant molecular clouds (GMCs; McKee & Ostriker 2007), yet only emits directly at high temperatures, it is nearly invisible via direct emission in these environments and thus must be traced using the next most abundant molecule, carbon monoxide (CO). After measuring the velocity-integrated CO luminosity in a GMC (L'_{CO}), the corresponding molecular gas mass (M_{gas}) can be estimated by using the CO-to-H_2 conversion factor (α_{CO}), defined as $\alpha_{CO} = M_{gas}/L'_{CO}$ (Bolatto et al. 2013; Carleton et al. 2017). Owing to the large number of studies of this factor in the Milky Way that converge on a characteristic value of $\alpha_{CO,MW} = 4.4\ M_\odot pc^{-2}(K\ km/s)^{-1}$ (Narayanan & Hopkins 2013; Bolatto et al. 2013), extragalactic studies often adopt this Milky Way value for α_{CO} across all galaxies.

Since systematic variations of α_{CO} with various ISM properties are both expected and observed (Strong et al. 2004; Narayanan et al. 2012; Sandstrom et al. 2013), in this section we will explore how the common assumption that $\alpha_{CO} = \alpha_{CO,MW}$ will impact the inferred molecular gas in massive gas-rich quiescent galaxies. All values needed to calculate $\alpha_{CO} = M_{gas}/L'_{CO}$ are computed in post-processing using the SLICK code (Garcia et al. 2024), which derives model CO luminosities by splitting up each gas particle into concentric radial zones (Popping et al. 2019) and computing thermal, radiative, and statistical equilibrium throughout the sub-grid model

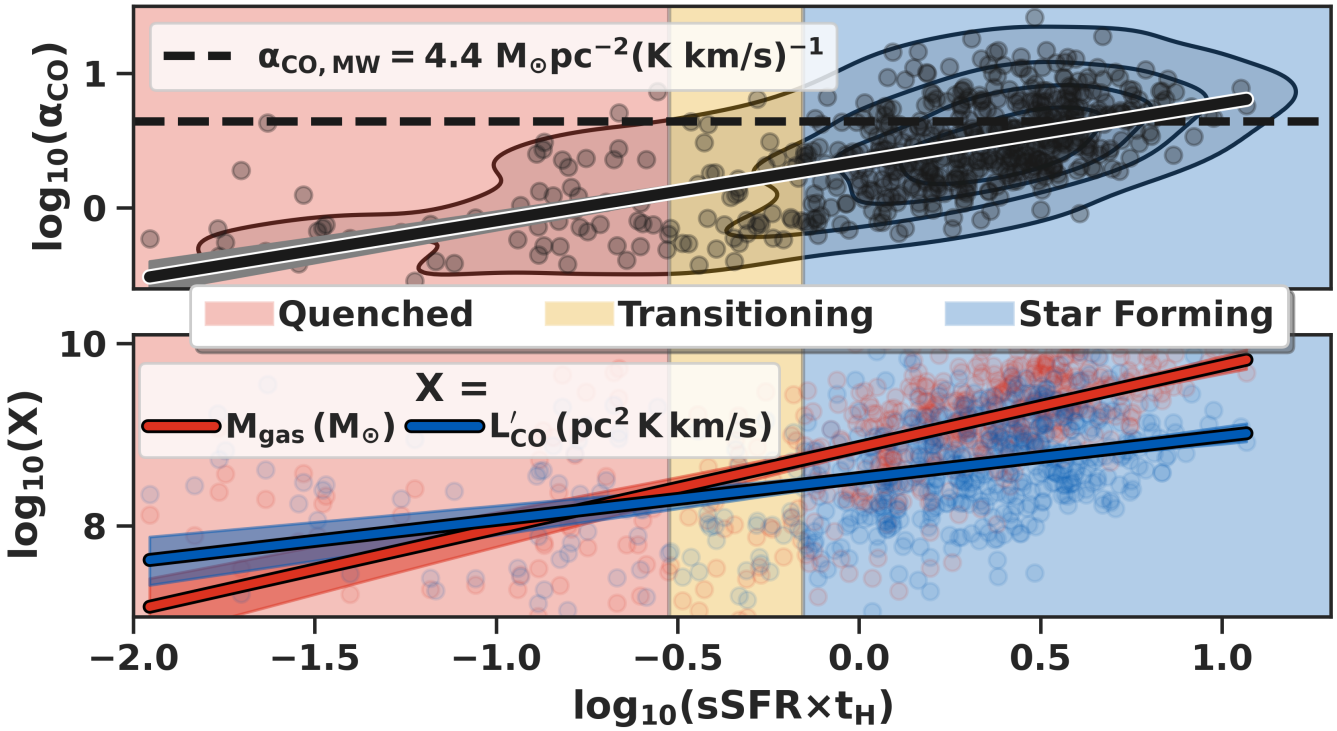


Figure 6. (Top) The value of α_{CO} increases with sSFR $\times$ t_H such that systems with low levels of star-formation will typically have a less than MW-like value of the CO-H_2 conversion factor ($\alpha_{CO} < \alpha_{CO,MW}$), implying observers who assume $\alpha_{CO} = \alpha_{CO,MW}$ would overestimate M_{H_2}. All massive ($M_* > 3 \times 10^9 M_\odot$) galaxies are shown here for $z = 0, 1$, with their logarithmic value of sSFR $\times$ t_H on the x-axis and α_{CO} on the y-axis (in units $M_\odot\ pc^{-2}(K\ km/s)^{-1}$). As in previous plots, the background shading corresponds to our star-forming classification scheme from §2.3.1, in which the blue background corresponds to galaxies that are star-forming (Eq. 2), yellow for transitioning (Eq. 3), and red for quenched (Eq. 4). The black line shown here is a linear regression model fit to our data, while the shaded region surrounding it is the associated 95% confidence interval, estimated using bootstrap resampling. From this, we see a trend in which α_{CO} is lower than $\alpha_{CO,MW}$ for quenched and transitioning galaxies, and only surpasses this for the most actively star-forming galaxies (sSFR $\times$ $t_H > 5$). **(Bottom) The reason that higher levels of star-formation correlate with higher α_{CO} stems from the fact that as a function of increasing sSFR $\times$ t_H, the gas mass (red line) in a galaxy will increase at a faster rate than the integrated CO luminosity (blue line).** While higher levels of star-formation are correlated with both an increase in H_2 and CO abundances, the decreasing temperatures that result from molecular gas shielding in dense star-forming regions lowers the rate at which the CO luminosity (L'_{CO}) will increase with respect to the gas mass (M_{gas}).

using DESPOTIC[3](Krumholz 2014). In this formalism, each gas particle can be thought of as representing a giant molecular cloud (GMC).

The molecular gas (M_{gas}) in our model assumes a GMC composition of molecular Hydrogen (H_2) and atomic Helium (He), in which the Helium mass is 40% of H_2, so that $M_{gas} \equiv M_{H_2} + M_{H_e} = M_{H_2}(1 + 0.4) = 7M_{H_2}/5$. Then to calculate α_{CO} for a galaxy in our simulation, we computed the total molecular gas mass of each gas particle that converged in post-processing, add their velocity-integrated CO luminosities, and obtain their ratio to get α_{CO}.

[3] DESPOTIC is a code to Derive the Energetics and SPectra of Optically Thick interstellar Clouds and can be found at https://bitbucket.org/krumholz/despotic/src/master/.

To investigate the relationship between the resulting α_{CO} of a galaxy and its level of star-formation, we show both quantities on a logarithmic scale for all $z = 0, 1$ massive ($M_* > 3 \times 10^9 M_\odot$) galaxies in Fig. 6. Here, the top panel shows α_{CO} on the y-axis and sSFR $\times$ t_H on the x-axis, while the bottom panel on the y-axis instead shows the numerator/denominator of α_{CO} in red/blue. As in the last section, the background shading corresponds to our star-forming classification scheme from Eq. 2.3.1, so that the blue background corresponds to galaxies that are star-forming (Eq. 2), yellow for transitioning (Eq. 3), and red for quenched (Eq. 4). In both panels, we fit a linear regression to the data and show the resulting relationship as a solid line, surrounded by a 95% confidence interval (estimated using bootstrap resampling). From the top panel in Fig. 6, we see that as a

galaxies level of star-formation increases (quantified by sSFR $\times$ t_H; c.f. §2.3.1), as does its value of α_{CO}. Furthermore, we see that all quenched, transitioning, and weakly star-forming galaxies will tend to have a value of α_{CO} less than $\alpha_{CO,MW}$, implying that the assumption that $\alpha_{CO} = \alpha_{CO,MW}$ in most recently quenched massive galaxies will cause an overestimated value of M_{H_2}. In fact, the linear regression shows that $\alpha_{CO} > \alpha_{CO,MW}$ only for galaxies with sSFR $\times$ $t_H > 5$.

In the bottom panel of Fig. 6, we show the linear regressions of both the numerator (M_{gas}) and denominator (L'_{CO}) of α_{CO} as red and blue lines, respectively, in order to better visualize the relationships between L'_{CO} and M_{gas} vs sSFR$\times t_H$. The CO luminosity, in optically thick gas, scales with the molecular gas velocity dispersion and temperature (Narayanan et al. 2012; Narayanan & Hopkins 2013). Galaxies that are quenched in our models tend to have lower column density ISM conditions, which result in warmer gas temperatures. This results in higher L'_{CO} per unit gas mass, driving the conversion factor below the Milky-Way mean value. We can broadly conclude that the recently quenched galaxies will tend to have $\alpha_{CO} < \alpha_{CO,MW}$, such that any observations that assume $\alpha_{CO} = \alpha_{CO,MW}$ may overestimate the H_2 mass.

3.3. *Hypothesis C: Dust Obscuration*

Our third hypothesis is that massive galaxies that appear to be quenched, but are rich in molecular gas, are actually harboring dust-obscured star formation, and are not actually quenched at all (e.g., Baron et al. 2022; Baron et al. 2023; Zhu et al. 2025; Cenci et al. 2025). Specifically, Baron et al. (2023) analyzed NOEMA CO(1-0) observations of 15 post-starburst galaxies with a multiwavelength approach, finding that while some regions of the galaxy are indeed quenched, other parts of the galaxy are instead forming stars in highly obscured regions.

In contrast to the previous two hypotheses, in this section we instead select our sample of galaxies based on their colors instead of their SFR, as we are testing whether or not star-forming galaxies can mimic signatures of quenched galaxies in their observational spectra (in other words: in order to fully test this hypothesis, we need to select low star-forming galaxies in a manner similar to observers). To accomplish this, we utilize the UBV-classification scheme described in §2.3.2.

After identifying which galaxies will satisfy our UBV-selection (Eq. 5) at $z = 0.5$ (red points in Fig. 2), we continue to investigate how the SFR derived from the IR deviates from the SFR derived from the FUV, as well as how both compare to the true SFR. Since most SFR indicators are derived from rest-UV or optical measurements, these methods are likely to yield lower SFR estimates than expected in dust-rich systems, as a significant portion of the high-energy radiation from the galaxy is absorbed by dust and re-emitted in the infrared. To test this hypothesis, we take our sample of UBV-selected galaxies (red points in Fig. 2) and calculate the SFR of these galaxies derived from their mock IR and far-UV photometry, to compare with the true SFR of the galaxies, with corresponding results shown in Fig. 7.

Following Murphy et al. (2011), we define L_{IR} as the integrated luminosity of our dust-attenuated SED from 8-1000μm, and convert it to an IR-based star-formation rate using $SFR_{IR}/(M_\odot/yr) = 3.88 \times 10^{-44} L_{IR}/(erg/s)$. Similarly, we define L_{FUV} by convolving the SED with a GALEX FUV transmission curve, and compute the corresponding FUV-based star-formation rate as $SFR_{FUV}/(M_\odot/yr) = 4.42 \times 10^{-44} L_{FUV}/(erg/s)$.

The results of applying this analysis to our sample of UBV-selected galaxies at $z = 0.5$ are shown in Fig. 7. Here, we show all UBV-selected selected systems (with $M_* > 3 \times 10^9 M_\odot$), colored by their dust mass. Additionally, for context, we also show as contours the non UBV-selected systems, split by whether they are star-forming (Eq. 2; sSFR $\times$ $t_H > 0.7$) or quenched (Eq. 4; sSFR $\times$ $t_H < 0.3$). In Fig. 7, the left-most panel shows a direct comparison of FUV-based SFR vs IR-based SFR, showing an excess of dust-obscured star formation for those UBV-selected systems that are also dust-rich. The middle plot shows the IR-based SFR vs true SFR, and demonstrates that the dust-rich UBV-selected galaxies have IR luminosities that accurately trace their true SFRs, while the IR luminosity of dust-poor galaxies is a less reliable indicator of true SFR. Finally, the right-most plot shows FUV-based SFR vs true SFR, and shows that while the UV luminosity severely underestimates the true SFR for all UBV-selected systems, it has the least severe effect for the most dust-poor systems. In all panels we see that among our UBV-selected galaxies, those that are dust-rich seem to mimic the trends of normal star-forming galaxies, while those dust-poor systems instead tend to have SFRs more similar to quenched systems.

From Fig. 7, see that while the IR-based SFR accurately traces the true SFR only in the most dust-rich systems, the FUV-based SFR has the opposite trend, in which the best agreement with true SFR occurs for the most dust-poor systems. This makes sense given that dust emits primarily in the IR, so the most dust-rich systems in our UBV-selected sample are absorbing all their UV energy, reprocessing it into the higher wavelength

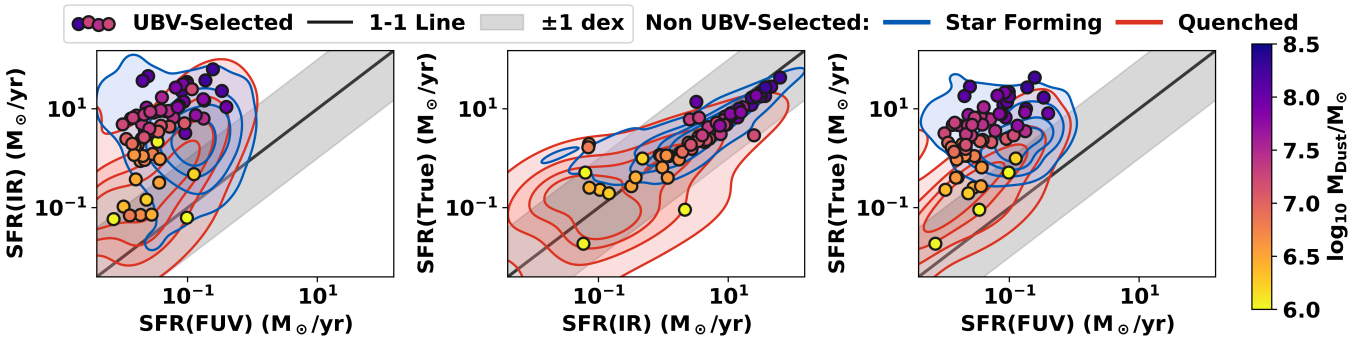


Figure 7. UBV-selected massive galaxies at $z = 0.5$ have an IR-based SFR that accurately traces their true SFR, yet a FUV-based SFR that significantly underestimates it. The left plot shows that among the UBV-selected galaxies, those that are most dust-rich will have an excess of dust-obscured star formation, which shifts the emitted UV starlight into the IR. As a result, the IR luminosity traces the SFR in these systems (middle plot), while the UV luminosity severely underestimates it (right plot). In contrast, the UV-based SFR works best for the most dust-poor systems, for which the IR-based SFR is the least reliable for.

IR emission, which then faithfully traces the true SFR. This is also why the most dust-poor systems have the best agreement between FUV-based SFR and true SFR. These findings are in contradiction with the assumption that UBV-selection will target relatively dust-free galaxies. Furthermore, from Fig. 2, we can also see that the most dust-rich galaxies also have the largest molecular and stellar masses.

Thus, from Fig. 7 we have now shown that among those galaxies that satisfy the PSB-like UBV criteria (Eq. 5) at $z = 0.5$, those that are most massive tend to be significantly more dust obscured than their low-mass counterparts. We continue by asking how this trend evolves with redshift by investigating how the extinction properties of the three populations shown in Fig. 7 evolve with redshift. This is accomplished in Fig. 8, in which for $z = 0, 1, 2$ we plot the KDE distribution of the visual optical depth ($\tau_V \equiv A_V * [2.5 \log_{10} e]^{-1}$). We approximated τ_V by using the value of the total extinction at $\lambda = 0.55\mu$m $= 5500$Å. As a result, it follows that $\tau_V \equiv \tau_\lambda(0.55\mu\text{m}) = \left(\frac{\ln 10}{2.5}\right) \times A_\lambda(0.55\mu\text{m})$. Furthermore, each distribution is scaled so that its peak equals one; therefore curve heights do not reflect relative numbers of galaxies, which are instead given in each panel's legend.

Within each plot in Fig. 8, we show the peak-normalized distributions of the optical attenuation for all UBV-selected galaxies (Eq. 5) in our simulation as a black line, those that are not UBV-selected and defined as star-forming according to Eq. 2 are shown as a blue line, and those that are not UBV-selected and defined as quenched according to Eq. 4 are shown as the red line. In Fig. 8, we see that at all redshifts, the UBV-selected galaxies have an optical attenuation that tracks that of non UBV-selected star-forming systems, and has significantly higher values of τ_V then the non UBV-selected quenched systems. Furthermore, we find that the optical attenuation of UBV-selected systems increases with increasing redshift, with a median τ_V that increases from 0.52 to 2.25 from $z = 0 \rightarrow 2$, showing how such systems will become more dust obscured at earlier times. In contrast, the median τ_V of the non UBV-selected and quenched systems decreases with increasing redshift, dropping from $\tau_V = 0.12 \rightarrow 0.04$ from $z = 0 \rightarrow 2$.

Collectively, the results of this section indicate that dust-obscured star formation may reasonably explain why observations are finding molecular gas in seemingly quenched galaxies. Using observationally-based selection criteria, we analyzed a sample of PSB-like galaxies and have shown that while a SFR derived from the FUV will underestimate the true SFR for all such galaxies, the IR-based SFR instead will accurately trace the true SFR for dust-rich galaxies (yet still underestimate it for dust-poor galaxies). We also found that such dust-rich galaxies will also have an abundance of gas and stars (Fig. 2).

In summary, this section suggests that the seemingly quenched massive and molecular gas-rich galaxies that exhibit PSB signatures instead contain dust-obscured star formation hidden in the galaxies center; surrounded by a quenched, dusty, and optically-thin outskirt that enshrouds the dust and exhibits PSB signatures.

4. DISCUSSION: COMPARISON TO OTHER THEORETICAL MODELS

Large-volume hydrodynamic simulations have had great success in the past in reproducing many of the statistical trends seen in observations (Somerville & Davé 2015; Pillepich et al. 2017; Vogelsberger et al. 2019; Crain & van de Voort 2023). Cosmological simulations such as these thus provide a potentially powerful avenue towards learning how massive galaxies can preserve their

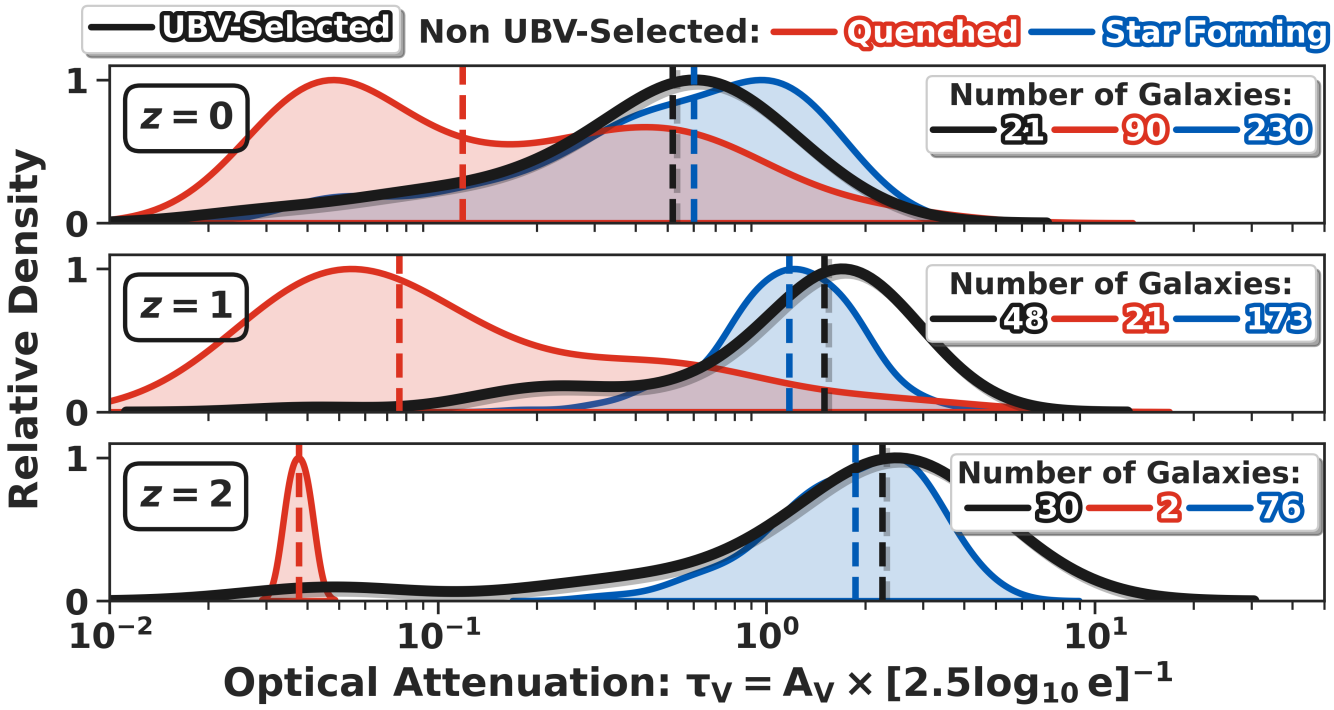


Figure 8. Massive ($M_* > 3 \times 10^9 M_\odot$) galaxies with PSB-like UBV colors (Eq. 5) have an optical attenuation similar to typical star-forming galaxies (Eq. 2), much higher than typical quenched galaxies (Eq. 4), with a value of τ_V that increases with redshift. Here, we show peak-normalized distributions of the visual optical depth (see legend for galaxy counts), calculated from attenuation curves, for our population of UBV-selected galaxies (black line), for our non UBV-selected star-forming galaxies (blue line), and for our non UBV-selected quenched galaxies (red line), to see how all three populations' extinction properties evolve with time. The median value for each population is shown as a dashed line.

molecular gas reservoirs after star formation shuts off. Throughout this paper we used the SIMBA simulation to investigate how molecular gas reservoirs could persevere in recently quenched massive galaxies.

To place our results in the context of previous work, this section reviews other theoretical studies of analogous systems, namely post-starburst galaxies (PSBs) as introduced in the introduction (§1). In this section we will focus on two major theoretical studies investigating the origin of molecular gas in PSBs. First, Davis et al. (2019) used the EAGLE simulations to investigate the molecular gas properties of PSBs, and secondly, Cenci et al. (2025) studied PSBs with the FIREBOX simulation (Feldmann et al. 2023), which is part of the *Feedback in Realistic Environments* (FIRE) project (Hopkins et al. 2014, 2018).

In terms of galaxy selection criteria, Davis et al. (2019) identified their sample of PSB galaxies in EAGLE by focusing on massive ($M_* \gtrsim 3.2 \times 10^9 M_\odot$) galaxies, initially star forming (sSFR $> 5 \times 10^{-11} yr^{-1}$), that experienced at least a factor of 5 drop in sSFR within 600 Myr. In contrast, Cenci et al. (2025) instead first used the same UBV-selection criteria applied in §3.3 to the central galaxies in FIREBOX with $M_* \geq 3 \times 10^9 M_\odot$ to define their sample of PSB galaxies. A 'true PSB' was then defined to be any such system with sSFR $< 3 \times 10^{-11} \mathrm{yr}^{-1}$, that also experienced a least a factor of four drop in their SFR since their most recent starburst, while an 'impostor PSB' would be any photometrically selected PSB that does not satisfy these additional criteria (i.e. UBV-selected but star-forming systems). This approach effectively combines aspects of our sSFR-based galaxy selection criteria described in §2.3.1 with the photometric selection method from §2.3.2.

Using these selection criteria, Cenci et al. (2025) found that among their star-forming galaxies, around 2.2% at $z = 0.7, 1.0$ would be classified as 'imposter PSBs', thus instead represent star-forming systems misclassified as PSBs due to their photometry, and will contain substantial molecular gas reservoirs with depletion times of 600 Myr – 1.2 Gyr. In contrast, those identified as 'true PSBs' (quenched and UBV selected) will be gas-poor, and will exhibit the longest depletion times. This is in line with our findings, in which among our UBV-selected systems (Eq. 5) at $z = 0.5$, those that are also star-forming (Eq. 2) will have median gas depletion timescales of 798 Myr, while those that are also quenched (Eq. 4) will have significantly longer depletion

timescales, with a median of ~ 2 Gyr. Similarly, Davis et al. (2019) found that the average PSB in EAGLE loses $\sim 90\%$ of its star-forming ISM within $\sim$600 Myr following the starburst.

Cenci et al. (2025) showed that typical PSBs, despite representing only 3.1% of $M_* > 3 \times 10^9 M_\odot$ galaxies at $z = 0.5, 1$, tend to have molecular gas contents similar to star-forming galaxies of similar mass. Of these, only $\sim$32% are classified as 'true PSBs'. Such systems are found to be significantly gas-poor, with typical gas reservoirs likely below the detection limits of current observational facilities, making these systems virtually undetectable. Thus, since a majority of PSBs in EAGLE retain significant molecular gas reservoirs (Davis et al. 2019), it would follow that such systems may instead constitute a sample of 'imposter PSBs', who have recently experienced a wave of feedback which has temporarily reduced their star forming efficiency. This is in line with their findings that such PSBs contain highly disturbed gas, with only a small fraction of kinetic energy in ordered rotation (Davis et al. 2019).

In the context of this study, it follows that in our analogous sample of UBV-selected 'PSB-like' galaxies defined in §2.3.2 (shown in Fig. 2), those dust-rich galaxies would be defined as 'impostor PSBs'. As discussed in §3.3, such systems likely have cores containing obscured star formation, surrounded by dusty outskirts that make their photometry resemble typical PSBs. The results from this section highlight that, in addition to the traditional photometric methods used to identify PSBs, to avoid including systems with dust-obscured ongoing star formation ('imposters'), one must incorporate additional selection criteria that focuses on their current level of star formation (in addition to their photometry).

5. CONCLUSION

The aim of this paper was to holistically investigate various hypotheses that could give rise to observations of massive ($M_* > 3 \times 10^9 M_\odot$) and quenched galaxies harboring significant molecular gas reservoirs such as those from Rowlands et al. (2015); French et al. (2015); Suess et al. (2017); Bezanson et al. (2022); Setton et al. (2025). The approach we took utilized the SIMBA hydrodynamic galaxy-formation simulations, whose novel multi-scale prescriptions have made it one of the best modern simulations for exploring galaxy evolution and baryon cycling within a cosmological context (Davé et al. 2019). Cosmological simulations such as this provide a powerful laboratory capable of studying the intricate interplay between a galaxy and its ISM, allowing in-depth investigations into their coevolution and the driving mechanisms connecting them.

While many studies have individually considered hypotheses that could give rise to observations of quenched galaxies that still harbor reservoirs of molecular gas, this study is meant to jointly investigate each within a singular cosmological simulation, providing a self-consistent analysis of the relative role of each theory across space and time. We investigated three hypotheses in total; the first of which asking about temporal effects intrinsic to the galaxy (§3.1), while the last two deal with observational effects. Specifically, our second hypothesis asks if the galaxy truly contains molecular hydrogen (§3.2), while the third asks if the galaxy is truly quenched (§3.3).

Our main results are as follows.

- **Hypothesis A: Temporary Quiescence (§3.1).** Rejuvenation among massive galaxies is most common for molecular gas-rich galaxies ($\sim$ 90% have $M_{\rm H_2}/M_* > 5\%$) that have not yet fully quenched ($\sim$ 80% are transitioning; Fig. 4). It is typically triggered by gas-rich mergers (Fig. 5), and is therefore most important at high redshift, becoming increasingly rare toward $z = 0$ (Fig. 3).

- **Hypothesis B: Incorrect $\alpha_{\rm CO}$ (§3.2).** Here, we showed that $\alpha_{\rm CO}$ declines with decreasing sSFR $\times$ $t_{\rm H}$, falling below $\alpha_{\rm CO,MW}$ for nearly all quenched, transitioning, and weakly star-forming galaxies (Fig. 6). Assuming a Milky Way-like $\alpha_{\rm CO}$ in these systems will thus lead to an overestimation in $M_{\rm H_2}$, most severely in the most quenched systems.

- **Hypothesis C: Dust Obscuration (§3.3).** Focusing on those galaxies that satisfy PSB-like quenching signatures (red dots in the top panel of Fig. 2), we show in Fig. 7 that those systems that are most dust-rich will have an IR-based SFR that accurately traces their true SFR, yet an FUV-based SFR that underestimates it. These findings, combined with the intuition from the bottom panel of Fig. 2 that the most dust-rich systems will also be the most massive and gas-rich, indicates that the UBV-selected molecular gas-rich systems from surveys like SQuiGG$\vec{L}$E could have star formation occurring deep within the galaxy, enshrouded by a quenched and dusty outskirt, with increasing levels of obscuration as redshifts increase (Fig. 8).

By investigating all three hypotheses, we conclude that each represent a plausible mechanism for contributing to the persistence of molecular gas in seemingly quenched galaxies, with their relative importance varying across redshift and ISM conditions. For example, at high redshift (around Cosmic Noon) galaxies are both

more likely to rejuvenate and host obscured star formation. A massive, gas-rich galaxy that rapidly quenched at these early times could therefore either return to star-forming activity if its molecular gas-to-stellar mass ratio is sufficiently high, or if sufficiently dusty, harbor obscured star formation that biases its photometric classification. At lower redshifts, by contrast, galaxies are more massive and easier to detect, but their α_{CO} values depart more severely from the canonical MW-like value, leading to increasingly overestimated molecular gas masses in more quenched systems.

In our discussion we put these results into the context of recent theoretical studies to show that such high-mass UBV-selected systems would actually be classified as 'imposter' PSBs due to their abundant and persistent molecular gas reservoirs. While existing observations seem to support this picture Setton et al. (2025), more results from ALMA are needed to fully understand the ISM conditions in these systems and to understand the relative role of each of our hypothesis across space and time.

Acknowledgments

D.N., R.B. and J.G. are grateful for funding from the NSF via grant AST-1908137. E.S. was additionally funded via grant NASA ADSPS23-0007. The authors acknowledge UFIT Research Computing for providing computational resources on HiPerGator and support that have contributed to the research results reported in this publication (http://it.ufl.edu/rc).

REFERENCES

Abramson, L. E., Kelson, D. D., Dressler, A., et al. 2014, ApJL, 785, L36, doi: 10.1088/2041-8205/785/2/L36

Akins, H. B., Narayanan, D., Whitaker, K. E., et al. 2022, The Astrophysical Journal, 929, 94, doi: 10.3847/1538-4357/ac5d3a

Alatalo, K., Lisenfeld, U., Lanz, L., et al. 2016, The Astrophysical Journal, 827, 106, doi: 10.3847/0004-637X/827/2/106

Alatalo, K., Bitsakis, T., Lanz, L., et al. 2017, ApJ, 843, 9, doi: 10.3847/1538-4357/aa72eb

Anglés-Alcázar, D., Davé, R., Faucher-Giguère, C.-A., Özel, F., & Hopkins, P. F. 2017, Monthly Notices of the Royal Astronomical Society, 464, 2840, doi: 10.1093/mnras/stw2565

Baron, D., Netzer, H., French, K. D., et al. 2023, Monthly Notices of the Royal Astronomical Society, 524, 2741, doi: 10.1093/mnras/stad1792

Baron, D., Netzer, H., Lutz, D., Prochaska, J. X., & Davies, R. I. 2022, MNRAS, 509, 4457, doi: 10.1093/mnras/stab3232

Baron, D., Netzer, H., Prochaska, J. X., et al. 2018, Monthly Notices of the Royal Astronomical Society, 480, 3993, doi: 10.1093/mnras/sty2113

Belli, S., Newman, A. B., & Ellis, R. S. 2019, The Astrophysical Journal, 874, 17, doi: 10.3847/1538-4357/ab07af

Bezanson, R., Spilker, J. S., Suess, K. A., et al. 2022, The Astrophysical Journal, 925, 153, doi: 10.3847/1538-4357/ac3dfa

Blanton, M. R., & Moustakas, J. 2009, ARA&A, 47, 159, doi: 10.1146/annurev-astro-082708-101734

Blanton, M. R., Hogg, D. W., Bahcall, N. A., et al. 2003, ApJ, 594, 186, doi: 10.1086/375528

Bluck, A. F. L., Maiolino, R., Piotrowska, J. M., et al. 2020, Monthly Notices of the Royal Astronomical Society, 499, 230, doi: 10.1093/mnras/staa2806

Bluck, A. F. L., Conselice, C. J., Ormerod, K., et al. 2023, Galaxy quenching at the high redshift frontier: A fundamental test of cosmological models in the early universe with JWST-CEERS. https://arxiv.org/abs/2311.02526

Bolatto, A. D., Wolfire, M., & Leroy, A. K. 2013, Annual Review of Astronomy and Astrophysics, 51, 207–268, doi: 10.1146/annurev-astro-082812-140944

Bondi, H. 1952, Monthly Notices of the Royal Astronomical Society, 112, 195, doi: 10.1093/mnras/112.2.195

Brammer, G. B., Whitaker, K. E., van Dokkum, P. G., et al. 2011, ApJ, 739, 24, doi: 10.1088/0004-637X/739/1/24

Calabrò, A., Daddi, E., Puglisi, A., et al. 2019, A&A, 623, A64, doi: 10.1051/0004-6361/201834522

Carleton, T., Cooper, M. C., Bolatto, A. D., et al. 2017, Monthly Notices of the Royal Astronomical Society, 467, 4886, doi: 10.1093/mnras/stx390

Carnall, A. C., McLure, R. J., Dunlop, J. S., & Davé, R. 2018, Monthly Notices of the Royal Astronomical Society, 480, 4379, doi: 10.1093/mnras/sty2169

Cenci, E., Feldmann, R., Wellons, S., et al. 2025, The Nature of Post-Starburst Galaxies: Real Deal or Masquerading Impostors? https://arxiv.org/abs/2509.00146

Choi, J., Dotter, A., Conroy, C., et al. 2016, ApJ, 823, 102, doi: 10.3847/0004-637X/823/2/102

Conroy, C., & Gunn, J. E. 2010, ApJ, 712, 833, doi: 10.1088/0004-637X/712/2/833
Conroy, C., Gunn, J. E., & White, M. 2009, ApJ, 699, 486, doi: 10.1088/0004-637X/699/1/486
Conroy, C., White, M., & Gunn, J. E. 2010, ApJ, 708, 58, doi: 10.1088/0004-637X/708/1/58
Conselice, C. J. 2007, in IAU Symposium, Vol. 235, Galaxy Evolution across the Hubble Time, ed. F. Combes & J. Palouš, 381–384, doi: 10.1017/S1743921306010222
Crain, R. A., & van de Voort, F. 2023, Annual Review of Astronomy and Astrophysics, 61, 473–515, doi: 10.1146/annurev-astro-041923-043618
Davé, R., Anglés-Alcázar, D., Narayanan, D., et al. 2019, MNRAS, 486, 2827, doi: 10.1093/mnras/stz937
Davé, R., Crain, R. A., Stevens, A. R. H., et al. 2020, MNRAS, 497, 146, doi: 10.1093/mnras/staa1894
Davis, T. A., van de Voort, F., Rowlands, K., et al. 2019, Monthly Notices of the Royal Astronomical Society, 484, 2447, doi: 10.1093/mnras/stz180
Davis, T. A., Alatalo, K., Bureau, M., et al. 2012, Monthly Notices of the Royal Astronomical Society, 429, 534, doi: 10.1093/mnras/sts353
Davé, R., Thompson, R., & Hopkins, P. F. 2016, Monthly Notices of the Royal Astronomical Society, 462, 3265, doi: 10.1093/mnras/stw1862
Donnari, M., Pillepich, A., Nelson, D., et al. 2019, Monthly Notices of the Royal Astronomical Society, 485, 4817, doi: 10.1093/mnras/stz712
D'Onofrio, V. R., Spilker, J. S., Bezanson, R., et al. 2025, ApJ, 990, 166, doi: 10.3847/1538-4357/adf5bd
Dotter, A. 2016, The Astrophysical Journal Supplement Series, 222, 8, doi: 10.3847/0067-0049/222/1/8
Dressler, A., & Gunn, J. E. 1983, ApJ, 270, 7, doi: 10.1086/161093
Dwek, E. 1998, ApJ, 501, 643, doi: 10.1086/305829
Ellison, S. L., Huang, Q., Yang, D., et al. 2025, Low redshift post-starburst galaxies host abundant HI reservoirs. https://arxiv.org/abs/2503.03066
Feldmann, R., Quataert, E., Faucher-Giguère, C.-A., et al. 2023, Monthly Notices of the Royal Astronomical Society, 522, 3831, doi: 10.1093/mnras/stad1205
Franx, M., van Dokkum, P. G., Förster Schreiber, N. M., et al. 2008, ApJ, 688, 770, doi: 10.1086/592431
French, K. D. 2021, Publications of the Astronomical Society of the Pacific, 133, 072001, doi: 10.1088/1538-3873/ac0a59
French, K. D., Yang, Y., Zabludoff, A., et al. 2015, The Astrophysical Journal, 801, 1, doi: 10.1088/0004-637X/801/1/1
French, K. D., Yang, Y., Zabludoff, A. I., & Tremonti, C. A. 2018a, The Astrophysical Journal, 862, 2, doi: 10.3847/1538-4357/aacb2d
French, K. D., Zabludoff, A. I., Yoon, I., et al. 2018b, The Astrophysical Journal, 861, 123, doi: 10.3847/1538-4357/aac8de
French, K. D., Smercina, A., Rowlands, K., et al. 2023, ApJ, 942, 25, doi: 10.3847/1538-4357/aca46e
Garcia, K., Narayanan, D., Popping, G., et al. 2024, The Astrophysical Journal, 974, 197, doi: 10.3847/1538-4357/ad642c
Goto, T. 2005, Monthly Notices of the Royal Astronomical Society, 357, 937, doi: 10.1111/j.1365-2966.2005.08701.x
—. 2007, Monthly Notices of the Royal Astronomical Society, 381, 187, doi: 10.1111/j.1365-2966.2007.12227.x
Hardcastle, M. J., Evans, D. A., & Croston, J. H. 2007, Monthly Notices of the Royal Astronomical Society, 376, 1849, doi: 10.1111/j.1365-2966.2007.11572.x
Harrold, J. E., Almaini, O., Pearce, F. R., et al. 2025, The role of mergers and rejuvenation in the buildup of the quiescent population at cosmic noon. https://arxiv.org/abs/2512.14599
Hopkins, P. F. 2015, Monthly Notices of the Royal Astronomical Society, 450, 53, doi: 10.1093/mnras/stv195
—. 2017, A New Public Release of the GIZMO Code. https://arxiv.org/abs/1712.01294
Hopkins, P. F., Kereš, D., Oñorbe, J., et al. 2014, Monthly Notices of the Royal Astronomical Society, 445, 581, doi: 10.1093/mnras/stu1738
Hopkins, P. F., & Quataert, E. 2011, Monthly Notices of the Royal Astronomical Society, 415, 1027, doi: 10.1111/j.1365-2966.2011.18542.x
Hopkins, P. F., Wetzel, A., Kereš, D., et al. 2018, Monthly Notices of the Royal Astronomical Society, 480, 800, doi: 10.1093/mnras/sty1690
Hunter, J. D. 2007, Computing in Science & Engineering, 9, 90, doi: 10.1109/MCSE.2007.55
Jin, S.-W., Gu, Q., Huang, S., Shi, Y., & Feng, L.-L. 2014, ApJ, 787, 63, doi: 10.1088/0004-637X/787/1/63
Kennicutt, Robert C., J. 1998, ApJ, 498, 541, doi: 10.1086/305588
Kimmig, L. C., Remus, R.-S., Seidel, B., et al. 2025, ApJ, 979, 15, doi: 10.3847/1538-4357/ad9472
Kriek, M., Labbé, I., Conroy, C., et al. 2010, ApJL, 722, L64, doi: 10.1088/2041-8205/722/1/L64
Krumholz, M. R. 2014, MNRAS, 437, 1662, doi: 10.1093/mnras/stt2000
Krumholz, M. R., & Gnedin, N. Y. 2011, ApJ, 729, 36, doi: 10.1088/0004-637X/729/1/36

Krumholz, M. R., McKee, C. F., & Tumlinson, J. 2009, ApJ, 693, 216, doi: 10.1088/0004-637X/693/1/216
Laporte, N., Meyer, R. A., Ellis, R. S., et al. 2021, Monthly Notices of the Royal Astronomical Society, 505, 3336, doi: 10.1093/mnras/stab1239
Li, Q., Narayanan, D., & Davé, R. 2019, MNRAS, 490, 1425, doi: 10.1093/mnras/stz2684
Licquia, T. C., & Newman, J. A. 2015, ApJ, 806, 96, doi: 10.1088/0004-637X/806/1/96
Lotz, M., Dolag, K., Remus, R.-S., & Burkert, A. 2021, MNRAS, 506, 4516, doi: 10.1093/mnras/stab2037
Lotz, M., Remus, R.-S., Dolag, K., Biviano, A., & Burkert, A. 2019, MNRAS, 488, 5370, doi: 10.1093/mnras/stz2070
Martig, M., Bournaud, F., Teyssier, R., & Dekel, A. 2009, ApJ, 707, 250, doi: 10.1088/0004-637X/707/1/250
McDermid, R. M., Alatalo, K., Blitz, L., et al. 2015, Monthly Notices of the Royal Astronomical Society, 448, 3484, doi: 10.1093/mnras/stv105
McKee, C. F., & Ostriker, E. C. 2007, ARA&A, 45, 565, doi: 10.1146/annurev.astro.45.051806.110602
McKinnon, R., Torrey, P., & Vogelsberger, M. 2016, MNRAS, 457, 3775, doi: 10.1093/mnras/stw253
Merlin, E., Fortuni, F., Torelli, M., et al. 2019, Monthly Notices of the Royal Astronomical Society, 490, 3309, doi: 10.1093/mnras/stz2615
Murphy, E. J., Condon, J. J., Schinnerer, E., et al. 2011, The Astrophysical Journal, 737, 67, doi: 10.1088/0004-637X/737/2/67
Muzzin, A., Marchesini, D., Stefanon, M., et al. 2013, The Astrophysical Journal, 777, 18, doi: 10.1088/0004-637x/777/1/18
Narayanan, D., & Hopkins, P. F. 2013, Monthly Notices of the Royal Astronomical Society, 433, 1223, doi: 10.1093/mnras/stt784
Narayanan, D., Krumholz, M. R., Ostriker, E. C., & Hernquist, L. 2012, Monthly Notices of the Royal Astronomical Society, 421, 3127, doi: 10.1111/j.1365-2966.2012.20536.x
Narayanan, D., Turk, M. J., Robitaille, T., et al. 2021, The Astrophysical Journal Supplement Series, 252, 12, doi: 10.3847/1538-4365/abc487
Noeske, K. G., Weiner, B. J., Faber, S. M., et al. 2007, ApJL, 660, L43, doi: 10.1086/517926
Pacifici, C., Kassin, S. A., Weiner, B. J., et al. 2016, ApJ, 832, 79, doi: 10.3847/0004-637X/832/1/79
Parente, M. 2025, Modeling Dust in Galaxy Evolution Simulations. https://arxiv.org/abs/2504.10585
Park, M., Belli, S., Conroy, C., et al. 2024, Widespread rapid quenching at cosmic noon revealed by JWST deep spectroscopy. https://arxiv.org/abs/2404.17945
Pillepich, A., Springel, V., Nelson, D., et al. 2017, Monthly Notices of the Royal Astronomical Society, 473, 4077, doi: 10.1093/mnras/stx2656
Poggianti, B. M., & Barbaro, G. 1997, A&A, 325, 1025, doi: 10.48550/arXiv.astro-ph/9703067
Popping, G., Narayanan, D., Somerville, R. S., Faisst, A. L., & Krumholz, M. R. 2019, MNRAS, 482, 4906, doi: 10.1093/mnras/sty2969
Remus, R.-S., & Kimmig, L. C. 2023, Relight the Candle: What happens to High Redshift Massive Quenched Galaxies. https://arxiv.org/abs/2310.16089
Robitaille, T. P. 2011, A&A, 536, A79, doi: 10.1051/0004-6361/201117150
Rodríguez Montero, F., Davé, R., Wild, V., Anglés-Alcázar, D., & Narayanan, D. 2019, MNRAS, 490, 2139, doi: 10.1093/mnras/stz2580
Rowlands, K., Wild, V., Nesvadba, N., et al. 2015, MNRAS, 448, 258, doi: 10.1093/mnras/stu2714
Saintonge, A., Kauffmann, G., Wang, J., et al. 2011, Monthly Notices of the Royal Astronomical Society, 415, 61, doi: 10.1111/j.1365-2966.2011.18823.x
Saintonge, A., Tacconi, L. J., Fabello, S., et al. 2012, The Astrophysical Journal, 758, 73, doi: 10.1088/0004-637X/758/2/73
Sánchez-Blázquez, P., Peletier, R. F., Jiménez-Vicente, J., et al. 2006, MNRAS, 371, 703, doi: 10.1111/j.1365-2966.2006.10699.x
Sandstrom, K. M., Leroy, A. K., Walter, F., et al. 2013, ApJ, 777, 5, doi: 10.1088/0004-637X/777/1/5
Schmidt, M. 1959, ApJ, 129, 243, doi: 10.1086/146614
Setton, D. J., Dey, B., Khullar, G., et al. 2023, The Astrophysical Journal Letters, 947, L31, doi: 10.3847/2041-8213/acc9b5
Setton, D. J., Spilker, J. S., Bezanson, R., et al. 2025, SQuIGG$\vec{L}$E: Buried star formation cannot explain the rapidly fading CO(2-1) luminosity in massive, $z \sim 0.7$ post-starburst galaxies. https://arxiv.org/abs/2509.00148
Siegel, J., Setton, D., Greene, J., et al. 2024, UNCOVER: Significant Reddening in Cosmic Noon Quiescent Galaxies. https://arxiv.org/abs/2409.11457
Smercina, A., Smith, J.-D. T., French, K. D., et al. 2022, ApJ, 929, 154, doi: 10.3847/1538-4357/ac5d5f
Snyder, G. F., Cox, T. J., Hayward, C. C., Hernquist, L., & Jonsson, P. 2011, ApJ, 741, 77, doi: 10.1088/0004-637X/741/2/77
Somerville, R. S., & Davé, R. 2015, ARA&A, 53, 51, doi: 10.1146/annurev-astro-082812-140951

Speagle, J. S., Steinhardt, C. L., Capak, P. L., & Silverman, J. D. 2014, ApJS, 214, 15, doi: 10.1088/0067-0049/214/2/15

Spilker, J. S., Hayward, C. C., Marrone, D. P., et al. 2022, ApJL, 929, L3, doi: 10.3847/2041-8213/ac61e6

Spilker, J. S., Whitaker, K. E., Narayanan, D., et al. 2025, Unusually High Gas-to-Dust Ratios Observed in High-Redshift Quiescent Galaxies. https://arxiv.org/abs/2507.16914

Springel, V., & Hernquist, L. 2003, MNRAS, 339, 289, doi: 10.1046/j.1365-8711.2003.06206.x

Strong, A. W., Moskalenko, I. V., Reimer, O., Digel, S., & Diehl, R. 2004, A&A, 422, L47, doi: 10.1051/0004-6361:20040172

Suess, K. A., Bezanson, R., Spilker, J. S., et al. 2017, ApJL, 846, L14, doi: 10.3847/2041-8213/aa85dc

Suess, K. A., Kriek, M., Price, S. H., & Barro, G. 2021, ApJ, 915, 87, doi: 10.3847/1538-4357/abf1e4

Suess, K. A., Kriek, M., Bezanson, R., et al. 2022, The Astrophysical Journal, 926, 89, doi: 10.3847/1538-4357/ac404a

Suess, K. A., Beverage, A. G., Kriek, M., et al. 2025, Cold gas in a post-starburst pair at z 1.4: major mergers as a pathway to quenching in the HeavyMetal survey. https://arxiv.org/abs/2506.14361

Szomoru, D., Franx, M., van Dokkum, P. G., et al. 2013, ApJ, 763, 73, doi: 10.1088/0004-637X/763/2/73

Szpila, J., Davé, R., Rennehan, D., Cui, W., & Hough, R. T. 2025, MNRAS, 537, 1849, doi: 10.1093/mnras/staf132

Tacchella, S., Carollo, C. M., Renzini, A., et al. 2015, Science, 348, 314, doi: 10.1126/science.1261094

Tacchella, S., Conroy, C., Faber, S. M., et al. 2022, The Astrophysical Journal, 926, 134, doi: 10.3847/1538-4357/ac449b

Tacconi, L. J., Genzel, R., Saintonge, A., et al. 2018, ApJ, 853, 179, doi: 10.3847/1538-4357/aaa4b4

Thompson, R. 2014, pyGadgetReader: GADGET snapshot reader for python, Astrophysics Source Code Library, record ascl:1411.001

Torrey, P., Wellons, S., Machado, F., et al. 2015, Monthly Notices of the Royal Astronomical Society, 454, 2770–2786, doi: 10.1093/mnras/stv1986

Tran, K.-V. H., Franx, M., Illingworth, G. D., et al. 2004, ApJ, 609, 683, doi: 10.1086/421237

Turk, M. J., Smith, B. D., Oishi, J. S., et al. 2011, ApJS, 192, 9, doi: 10.1088/0067-0049/192/1/9

Umehata, H., Kubo, M., & Nakanishi, K. 2025, ApJL, 985, L8, doi: 10.3847/2041-8213/add1d4

Veilleux, S., Cecil, G., & Bland-Hawthorn, J. 2005, ARA&A, 43, 769, doi: 10.1146/annurev.astro.43.072103.150610

Vogelsberger, M., Marinacci, F., Torrey, P., & Puchwein, E. 2019, Cosmological Simulations of Galaxy Formation. https://arxiv.org/abs/1909.07976

Waskom, M. L. 2021, Journal of Open Source Software, 6, 3021, doi: 10.21105/joss.03021

Weaver, J. R., Davidzon, I., Toft, S., et al. 2023, A&A, 677, A184, doi: 10.1051/0004-6361/202245581

Whitaker, K. E., & Bezanson, R. 2026, Annual Review of Astronomy and Astrophysics, doi: https://doi.org/10.1146/annurev-astro-043024-121502

Whitaker, K. E., van Dokkum, P. G., Brammer, G., & Franx, M. 2012, ApJL, 754, L29, doi: 10.1088/2041-8205/754/2/L29

Whitaker, K. E., Franx, M., Leja, J., et al. 2014, ApJ, 795, 104, doi: 10.1088/0004-637X/795/2/104

Whitaker, K. E., Franx, M., Bezanson, R., et al. 2015, ApJL, 811, L12, doi: 10.1088/2041-8205/811/1/L12

Wild, V., Almaini, O., Dunlop, J., et al. 2016, MNRAS, 463, 832, doi: 10.1093/mnras/stw1996

Wild, V., Taj Aldeen, L., Carnall, A., et al. 2020, MNRAS, 494, 529, doi: 10.1093/mnras/staa674

Williams, R. J., Quadri, R. F., Franx, M., et al. 2010, ApJ, 713, 738, doi: 10.1088/0004-637X/713/2/738

Worthey, G., & Ottaviani, D. L. 1997, ApJS, 111, 377, doi: 10.1086/313021

Wuyts, S., Förster Schreiber, N. M., Lutz, D., et al. 2011, ApJ, 738, 106, doi: 10.1088/0004-637X/738/1/106

Yang, Y., Zabludoff, A. I., Zaritsky, D., & Mihos, J. C. 2008, ApJ, 688, 945, doi: 10.1086/591656

Yesuf, H. M., Faber, S. M., Trump, J. R., et al. 2014, ApJ, 792, 84, doi: 10.1088/0004-637X/792/2/84

Yesuf, H. M., & Ho, L. C. 2020, ApJ, 900, 107, doi: 10.3847/1538-4357/abaa43

Young, L. M., Scott, N., Serra, P., et al. 2014, Monthly Notices of the Royal Astronomical Society, 444, 3408, doi: 10.1093/mnras/stt2474

Zabludoff, A. I., Zaritsky, D., Lin, H., et al. 1996, ApJ, 466, 104, doi: 10.1086/177495

Zhu, P., Suess, K., Kriek, M., et al. 2025, Astrophysical Journal, 981, doi: 10.3847/1538-4357/adaf1c

Ángel Chandro-Gómez, del P. Lagos, C., Power, C., et al. 2025, Unveiling the properties and origin of massive quenched galaxies at $z \geq 2$ in the COLIBRE hydrodynamical simulations. https://arxiv.org/abs/2512.16208

APPENDIX

A. MERGER-DRIVEN REJUVENATION

In §3.1, while investigating whether the observed molecular gas in quenched galaxies could be due to them experiencing a temporary period of dormancy (followed by a rejuvenation), we stated that the rejuvenation event shown in Fig. 5 was driven by a major merging event. In this section, we provide proof of this by visually examining the galaxy at various points in time. To accomplish this, we pick eight points of interest during our galaxies evolution and show a projection plot of the gas density for each (shown in Fig. 10/11), labeled with a letter (A-H) that corresponds to the time/redshift indicated by the same letter in the middle of Fig. 9 below.

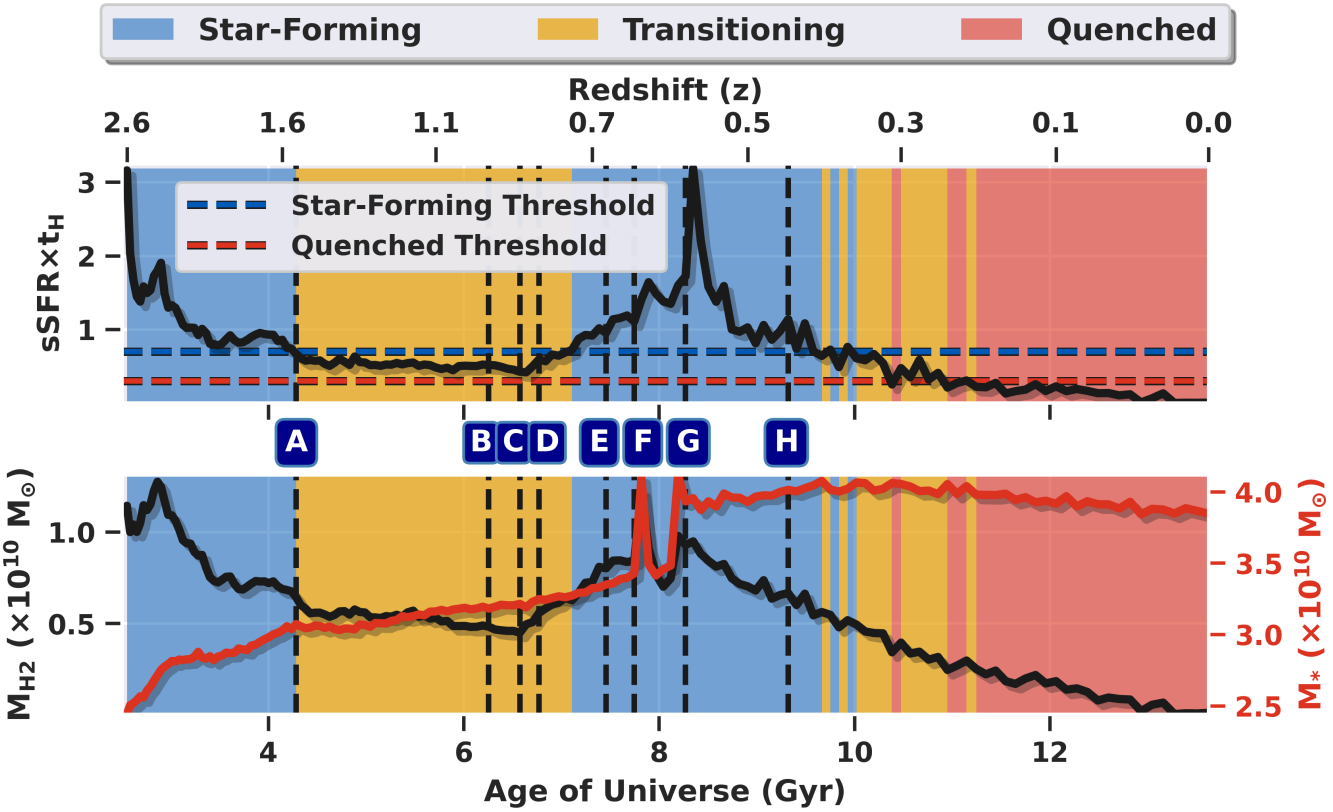


Figure 9. Example of the rejuvenating galaxy from Fig. 3 (§3.1), with added letters (A-H) corresponding to the images in Fig. 10/11. This galaxy was selected at $z \approx 1.5$ ('A': $t_H \sim 4.3$ Gyr), based on it satisfying both our conditions; having $M_* > 3 \times 10^9 M_\odot$ and sSFR $\times$ $t_H \leq 0.7$, with the background color set to the star-forming classification of the galaxy based on Eq. 2-4. While the top panel shows the evolution of sSFR $\times$ t_H, the bottom panel shows the corresponding evolution of H_2 mass (left/black) and stellar mass (right/red), both of which show a gradual evolution at high redshift, followed by a dramatic increase at around $z \approx 0.6$ driven by a major merging event. The drop-off after this and subsequent rise show that the merging galaxy initially passes through our main galaxy, but, now bound within its potential well, later falls back and ultimately merges.

As a reminder to the reader, in Fig. 9 (as in Fig. 5; §3.1), the top panel shows the quantity we used to classify the galaxy's current state of star formation (i.e. sSFR $\times$ t_H; see §2.3.1), thus has two horizontal lines located at (a) the star-forming cut (Eq. 2: sSFR $\times$ $t_H = 0.7$) and (b) the quenching threshold (Eq. 4: sSFR $\times$ $t_H = 0.3$). The background color in both panels reflects this classification, with blue regions showing where the system would be considered 'star-forming', yellow for 'transitioning', and red for 'quenched'. To investigate the external processes that influence this

galaxies evolution, we picked eight illustrative moments across time and produced a projection plot of the gas density in our galaxy for each (Fig. 10/11) via yt (Turk et al. 2011), an astrophysical analysis and visualization toolkit.

We begin our exploration of this galaxies evolution at a redshift of $z = 1.52$ (labeled 'A'; $t_H \sim 4.28$ Gyr), in which the previously star-forming galaxy has just had its SFR decrease into our transitioning phase of star formation (Eq. 3). In an isolated medium such a galaxy will continue towards quiescence, but in our cosmological simulation mergers can also occur. We see evidence of an interloper galaxy encroaching into the territory of our target galaxy in the top-right of the image labeled 'B' in Fig. 10 ($t_H = 6.26$ Gyr, $z = 0.92$). Moving forward in time, we can see in the same figure (Fig. 10) that this interloper passes directly through the center of our target galaxy in the images labeled 'C'/'D' around $t_H = 6.6$ Gyr. At the same time in Fig. 9, we see at the lines labeled 'C'/'D', that after this initial pass through, while stellar mass seems unaffected (red line), the H_2 mass (black line) of the galaxy begins to increase after this point ($t_H > 6.6$ Gyr). This behavior arises since by definition, gas is collisional while stars are not, thus in this initial pass through the gas in the two galaxies is the first to collide and collapse.

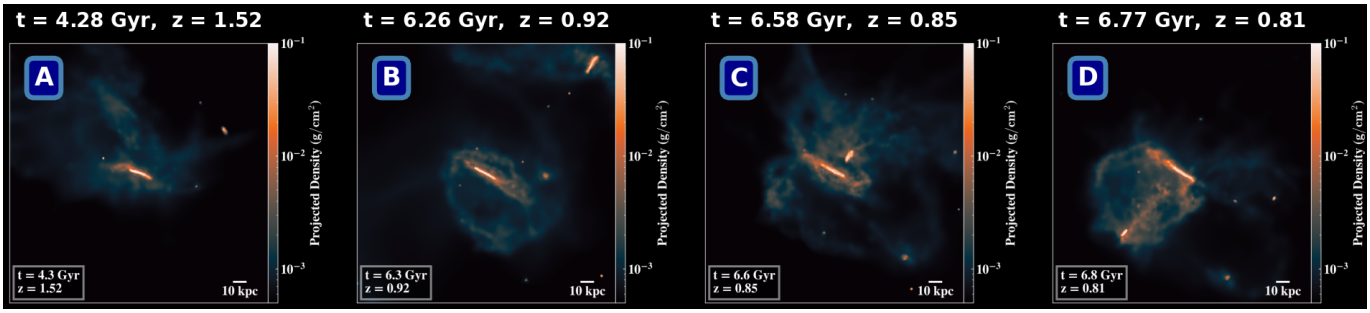


Figure 10. **A**: previously star-forming galaxy is beginning to quench; **B**: interloping galaxy enters the gravitational well of our target galaxy; **C**: interloping system falls into our target galaxy; **D**: interloping system falls through and past our target galaxy, replenishing the molecular gas in the galaxy.

Due to the high velocity of this initial galactic collision, the interloper galaxy does not immediately coalesce with our target galaxy. Instead, we see the interloper galaxy passes through and past our target galaxy, reaching a maximum distance from it at around 500 Myr after the initial pass-through, after which it begins to fall back into the gravitational well of our target galaxy, as shown in the image labeled 'E' in Fig. 11 ($t_H = 7.46$Gyr, $z = 0.69$). Around 300 Myr later is when the interloper galaxy finally falls back and begins its second pass through of our target galaxy. This can be seen in the image labeled 'F' in Fig. 11 ($t_H = 7.75$Gyr, $z = 0.64$). In the same moment of time in Fig. 9, at the line labeled 'F' we see this second pass through causes the galaxy tracker to briefly misidentify the galaxy, as it is not sure which galaxy is our primary during this turbulent collision. Regardless, this merger causes a rapid rise in stellar mass at the lines labeled 'F' and 'G' in Fig. 9 as the galaxy passes through a second time then eventually fully merges with our target galaxy, as seen in the image labeled 'G' in Fig. 11 ($t_H = 8.27$Gyr, $z = 0.56$).

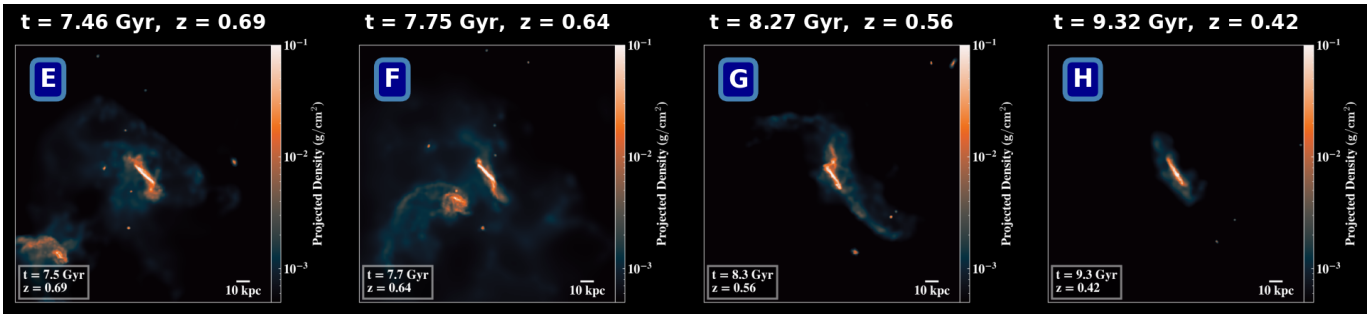


Figure 11. **E**: interloper galaxy, after first pass through, again begins to fall back into our target system; **F**: interloper galaxy falls back for its second pass through; **G**: interloper galaxy finally merges with our target galaxy; **H**: after merging, the combined systems heads towards quiescence.

In between the points labeled 'F' and 'G' in Fig. 9, we see a rapid increase in the SFR of our target galaxy, as it absorbs the gas and stars from the interloping system. After our target galaxy fully absorbs the merging system, its SFR is seen to reach a maximum value at $t_H = 8.35$ Gyr ($z = 0.55$), after which it again begins to fall towards quiescence. This galaxy will eventually deplete all of its newly replenished gas, and in our formalism is defined to be fully quenched by $t_H = 11.25$ Gyr ($z = 0.21$), after which it will continue as a typical elliptical galaxy towards complete quenching.

B. COMPARING SELECTION METHODS

B.1. *Comparing sSFR*t to distance from SFMS*

As discussed in §2.3.1, an alternative approach to distinguishing between star-forming and quenched galaxies is based on the galaxies offset from the majority of star-forming systems on a plot of stellar mass (M_*) vs star-formation rate (SFR). Typical star-forming galaxies have a well established relationship between M_* and SFR (known as the Star-Forming Main Sequence; SFMS; Noeske et al. 2007; Whitaker et al. 2012, 2014; Speagle et al. 2014). This relationship arises because galaxies that lie on the main sequence are in a quasi-equilibrium ('gas-regulated') state (Tacconi et al. 2018), in which their star formation is limited by the amount of molecular gas available (M_{H_2}) as well as the gas' efficiency at creating stars ($t_{dep} \equiv M_{H_2}/\mathrm{SFR}$ = depletion time; Saintonge et al. (2011)). To calculate the SFMS for our simulated galaxies, we followed the formalism of Whitaker et al. (2014) to fit a second-order polynomial to the running median of log SFR at each redshift. This was done iteratively, allowing us to fit the polynomial from Whitaker et al. (2014), given as

$$\log \mathrm{SFR_{MS}} = a + b\log(M_*/M_\odot) + c\log(M_*/M_\odot)^2 \approx \log\left(\frac{\text{Molecular Gas Mass } (M_{H_2})}{\text{Depletion Time } (t_{dep})}\right) \tag{B1}$$

The best fit coefficients from this model (a, b, c) were found to be $(-22.59, 4.03, -0.18)$ at $z = 0$, $(-20.23, 3.40, -0.13)$ at $z = 1$, $(-17.39, 2.68, -0.08)$ at $z = 2$, $(-14.25, 1.98, -0.04)$ at $z = 3$, and $(-3.86, -0.30, 0.08)$ at $z = 4$.

The resulting SFR from Eq. B1 therefore represents the expected SFR of a typical star-forming galaxy on the main sequence at a given stellar mass (M_*), and is shown in Fig. 1 (§2.3.1) as a solid black curve for our SIMBA galaxies. Due to this definition, it follows that comparing a galaxies true SFR to its expected main sequence SFR (SFMS; Eq. B1) can provide another method of classifying a galaxy by its level of star-formation. As a result, we continue to define how far below a galaxies true SFR is from its expected main sequence SFR using

$$\Delta\mathrm{SFMS\ (dex)} = \log_{10}(\mathrm{SFR_{MS}}) - \log_{10}(\mathrm{SFR_{True}}) = \log_{10}\left(\frac{\mathrm{SFR_{MS}}}{\mathrm{SFR_{True}}}\right) = \text{dex below SFMS} \tag{B2}$$

Using Eq. B2, we can now use the distance a galaxy's true SFR (Eq. 1) is below its main sequence SFR (Eq. B1) to quantify its level of quiescence. From Whitaker & Bezanson (2026), galaxies 1σ below the SFMS are typically 0.3 dex away, so 1 dex below would correspond to $\sim 3.3\sigma$. In this formalism, galaxies below the SFMS by $2-3\sigma$ ($0.6-0.9$ dex) would be considered 'transitioning', while those further than 0.9 dex below are conservatively quenched. To summarize, we find from Whitaker & Bezanson (2026) that galaxies can be classified by Eq. B2 like

$$\text{Star Forming}: \quad \Delta\mathrm{SFMS} \leq 0.6 \text{ dex} \tag{B3}$$

$$\text{Transitioning}: \quad 0.6 \text{ dex} < \Delta\mathrm{SFMS} < 0.9 \text{ dex} \tag{B4}$$

$$\text{Quenched}: \quad \Delta\mathrm{SFMS} \geq 0.9 \text{ dex} \tag{B5}$$

We show a direct comparison of this method of classifying galaxies versus our $\mathrm{sSFR} \times t_H$ method defined by Eq. 2-4 in Fig. 12 below. Here we show all $M_* > 3 \times 10^9 M_\odot$ galaxies in our sample for $z = 0-4$, with their value of $\mathrm{sSFR} \times t_H$ on the x-axis and their distance below the SFMS (Eq. B2) on the y-axis. We additionally added vertical and horizontal hatched regions corresponding to the 'quenched' and 'star-forming' regimes of both methods in red and blue respectively, with labels describing their meaning on the top/right. Additionally, in between each regime we have indicated via grey shading the area defined as 'transitioning'. Looking at Fig. 12, we see that our fiducial quenching threshold of $\mathrm{sSFR} \times t_H = 0.3$ roughly corresponds to 0.6 dex at $z = 0$ and 0.9 dex for $z > 0$.

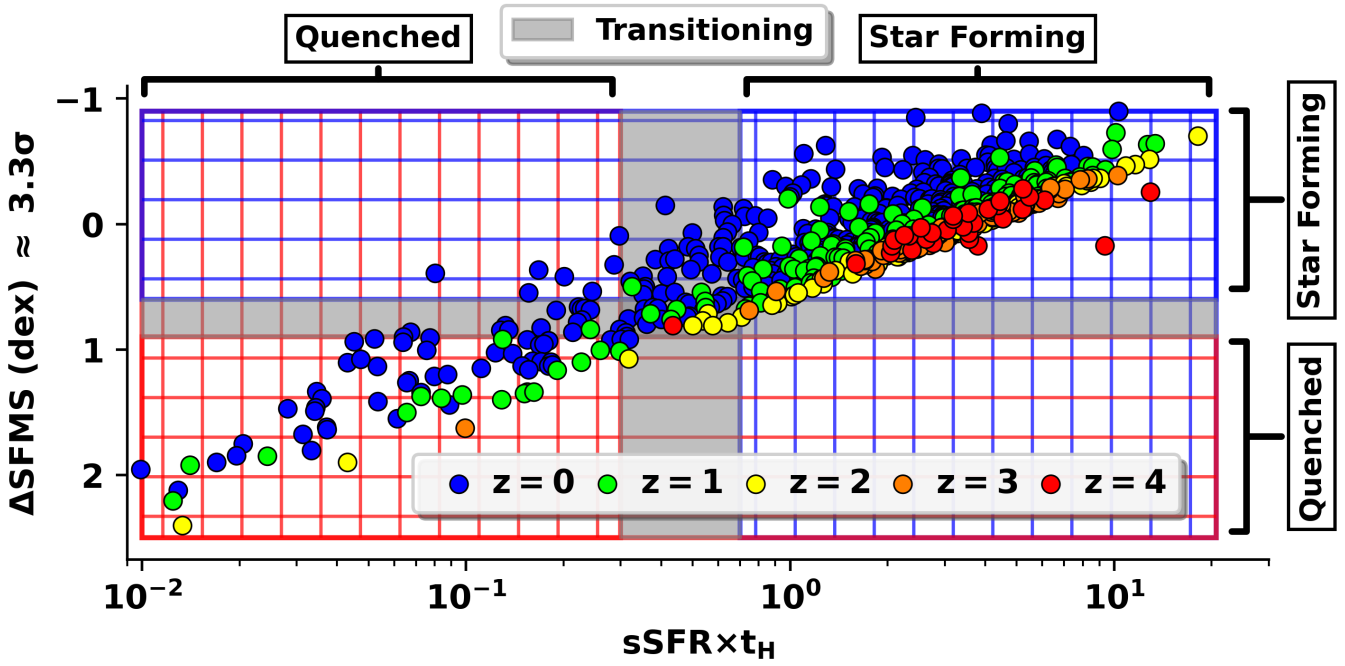


Figure 12. Direct comparison of the galaxy classification method described in §2.3.1 (used in §3.1/§3.2) vs the alternative SFMS-based classification described in this section. All $M_* > 3 \times 10^9 M_\odot$ galaxies are shown as dots, colored by their redshift, with their sSFR×t_H on the x-axis and their distance below the SFMS (Eq. B2) on the y-axis. The quenched/star-forming regions for each definition are shown via red/blue vertical and horizontal lines, with labels on the top/right of the axii, while the transitioning regime is indicated via grey shading.

Since our study is broadly interested in the properties of all non star-forming galaxies, we can combine our transitioning and quenched populations into one we can call 'low star forming'. From our fiducial definitions, it follows that 'low star-forming' galaxies are any with sSFR $\times$ t_H < 0.7. Using the SFMS-based definition, it follows that 'low star-forming' galaxies are any with ΔSFMS > 0.6 dex. Now we can compare how the 'low star-forming' galaxies used in our study compares with the analogous sample generated with the SFMS-based definition (Eq. B1). This comparison is shown via a a table of KDE distribution plots in Fig. 13. In each panel we show the distribution of $M_* > 3 \times 10^9 M_\odot$ galaxies identified to be 'low star forming' using our sSFR-based definition as a solid blue line, and the corresponding sample of 'low star forming' galaxies identified using ΔSFMS as a dashed blue line. In Fig. 13, the left column shows the distribution of stellar mass (M_*), the middle column shows the stellar-mass weighted molecular hydrogen gas mass (M_{H_2}), while the right-most column shows stellar-mass weighted star formation rate (SFR), which by definition is heavily dependent on M_{H_2} (Eq. 1). The top row shows data for $z = 0$, the middle for $z = 1$, and the bottom for $z = 2$.

Upon examining Fig. 13 we see two interesting effects. First, the stellar mass (left-most column) from the two samples is approximately equal for all redshift, and second; while both the H_2 mass and SFR agree for $z = 2$, they diverge at $z = 0$. It makes sense that both samples have the same stellar mass as both methods used stellar mass as fundamental inputs into their formalism (i.e. both sSFR and SFR_{MS} are calculated via M_*). Furthermore, despite neither method explicitly using M_{H_2}, we find their resulting M_{H_2} distributions are seemingly different for $z = 0$, with the sSFR method of selecting 'low star forming' galaxies producing a sample with higher molecular gas mass (and SFR) than the ΔSFMS method explored here. The reasoning for this is that, as explained at the beginning of this section, galaxies on the main sequence have their star-formation regulated by their available reservoir of H_2, so that galaxies below the main sequence will always be relatively depleted of molecular gas. In contrast, our sSFR-based definition of 'low star forming' galaxies introduces no analogous cut in molecular gas, allowing gas-rich systems with suppressed star forming efficiency to be included in our sample.

In summary, using our sSFR-based method of identifying 'low star forming' galaxies produces a sample of galaxies with higher molecular gas masses then the analogous sample selected using ΔSFMS. Thus, since the focus of our

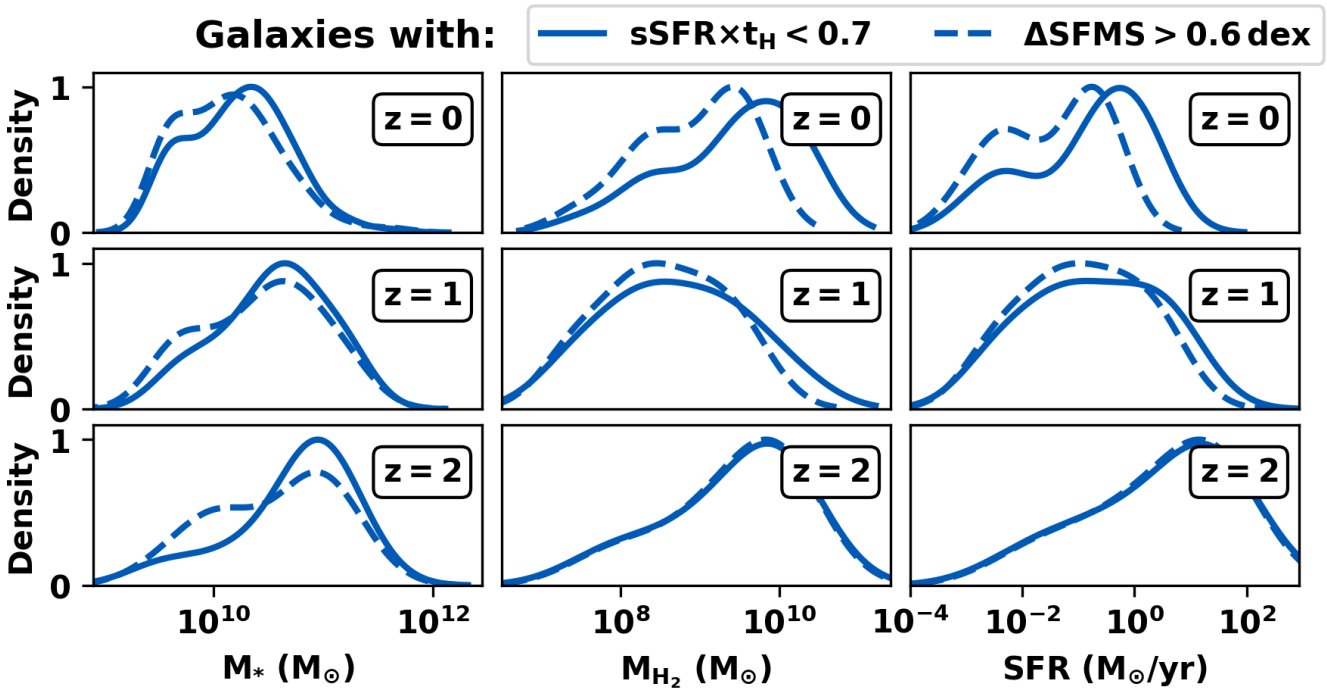


Figure 13. Both the sSFR and ΔSFMS classification methods show good agreement at $z > 0$, whereas substantial deviations exist at $z = 0$. In each panel we show the distribution of $M_* > 3 \times 10^9 M_\odot$ galaxies identified to be 'low star forming' using our sSFR-based definition (sSFR $\times$ $t_H < 0.7$) as a solid blue line and the corresponding sample of 'low star forming' galaxies identified using ΔSFMS (ΔSFMS > 0.6 dex) as a dashed blue line. The left column shows the distribution of stellar mass (M_*), the middle column shows molecular gas mass (M_{H_2}), while the right-most column shows SFR, which by definition is heavily dependent on the M_{H_2}. Each row is defined by a single redshift.

paper is on those 'low star forming' galaxies that are also molecular gas-rich, we stick with the sSFR-based method. Additionally, doing so avoids the need to iteratively fit the SFMS at every snapshot we investigate.

B.2. *UBV Selection Comparisons*

The sample of galaxies from Suess et al. (2022) comes from the Studying Quenching in Intermediate-z Galaxies: Gas, angu$\vec{L}$ar momentum, and Evolution (SQuiGG$\vec{L}$E) survey of intermediate-redshift PSBs from SDSS. From their initial sample of ∼32,000 galaxies from $z = 0.5 - 0.9$, applying their UBV cut specified above results in their final sample of ∼1,300 unique PSB systems. They find the majority of their systems are massive ($M_* \gtrsim 10^{11} M_\odot$), have SFRs below the main sequence, and formed more than 10% of their mass in a recent burst. This is by design, as SQuiGG$\vec{L}$E is meant to select bright, massive, and burst-dominated galaxies, but does not directly reflect the mass of typical PSBs, as lower mass systems could exist but would not have been bright enough to be included in this catalog. Furthermore, their final sample is also found to be associated with high Hδ_A equivalent widths (implying no ongoing star formation) and low Dn4000 indices (implying a young/hot/massive stellar population). When stacking all the spectra from their final sample, as shown as the black line in Fig. 15 (grey shading indicates the 16th-84th percentiles), they find there average SQuiGG$\vec{L}$E spectra will have a strong Balmer break, blue slopes redwards of this break, deep Balmer absorption lines, and typically weak or absent [OII] and [OIII] emission lines.

Now to compare their resulting sample against our analogous sample of UBV-selected galaxies (used in §3.3), we again show the top panel of Fig. 2, but now add to the plot the analogous galaxy sample used by Suess et al. 2022 (black dots). Upon examining Fig. 14, we see many differences between the two samples. First, we see that the SQuiGG$\vec{L}$E galaxies (black points) have much higher/redder values of $U_m - B_m$, which implies that SQuiGG$\vec{L}$E galaxies have a larger Balmer break and weaker UV emission than those UBV-selected systems in SIMBA (red points). Specifically, $U_m - B_m$ quantifies the contribution of young stars to the total light, so is a sensitive probe of recent star formation, which further implies that the SQuiGG$\vec{L}$E galaxies are also more burst dominated than those in SIMBA. As a result,

we see also on the right-panel of Fig. 14 that the fact that SIMBA galaxies (red points) are more dominated by recent star formation causes them to have significantly lower values of Lick Hδ_A than the SQuiGG$\vec{L}$E galaxies (black points).

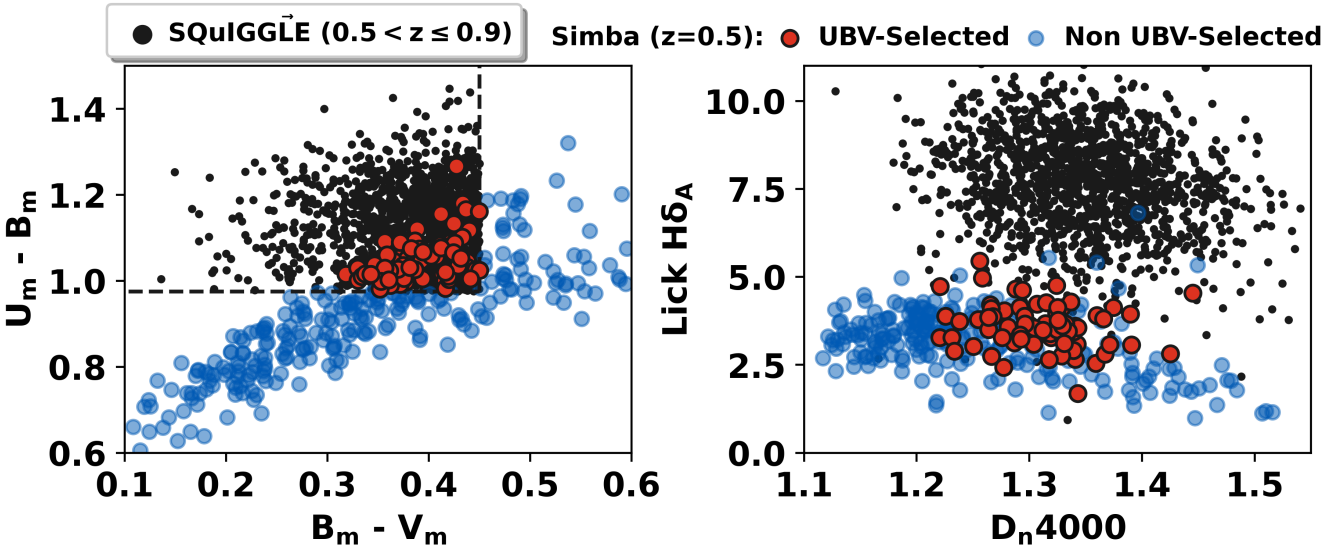


Figure 14. Same as top panel of Fig. 2, where red dots indicate those UBV-selected systems from SIMBA at $z = 0.5$, with the addition of galaxies from the SQuiGG$\vec{L}$E survey (black points), shows how SQuiGG$\vec{L}$E galaxies are generally redder than those UBV-selected SIMBA systems. As in the top panel of Fig. 2, the left-hand plot shows the galaxies in UBV space, defined by the medium-band rest-frame filters (U_m, B_m, and V_m), designed to target the Balmer break and slope of the spectrum redward of the break (Suess et al. 2022). Right-hand plot shows the galaxies lick Hδ_A index (Hδ EW; which traces recent star formation) as a function of the 4000Å break index (D_n4000; which probes the age of the stellar population).

This can be confirmed visually in in Fig. 15, in which we show a combined stack (normalized at 4500Å) of all ∼1,300 SQuiGG$\vec{L}$E galaxies as a solid black line, and the combined stack of our 72 UBV-selected ($z = 0.5$) SIMBA galaxies as a solid red line, with both lines surrounded by a shaded region indicating the 16th-84th percentile range of the spectra. Here we see that the SQuiGG$\vec{L}$E galaxies do have larger Balmer breaks than the corresponding SIMBA systems, as concluded above. Additionally, focusing on the location of the $H\delta$ absorption line (4101Å), we see that the SQuiGG$\vec{L}$E galaxies have significantly stronger Balmer-line absorption then the SIMBA galaxies. This arises from the fact that SQuiGG$\vec{L}$E are more burst-dominated than SIMBA , which makes sense as by design, SIMBA is not meant to include bursty star formation. The inability for SIMBA to produce 'bursty' star formation largely stems from its subgrid treatment of the interstellar medium (ISM), which imposes a resolution-dependent temperature floor to prevent artificial fragmentation below the simulation's mass resolution (Springel & Hernquist 2003; Davé et al. 2016; Davé et al. 2019). This effective equation of state stabilizes dense gas against collapse on unresolved scales, thereby smoothing star-formation variability in time.

Secondly, we also see that the SQuiGG$\vec{L}$E galaxies (black points) also have very similar values of $B_m - V_m$ when compared to the UBV-selected SIMBA systems (red points), implying that the SQuiGG$\vec{L}$E galaxies have similar slopes in their spectra redwards/rightwards of the Balmer break than the UBV-selected systems in SIMBA. This is also visually confirmed in Fig. 15, in which we see that redwards of the Balmer break (towards higher wavelengths) both spectral stacks have extraordinarily similar slopes, reflecting the similar $B_m - V_m$ distributions calculated for both samples.

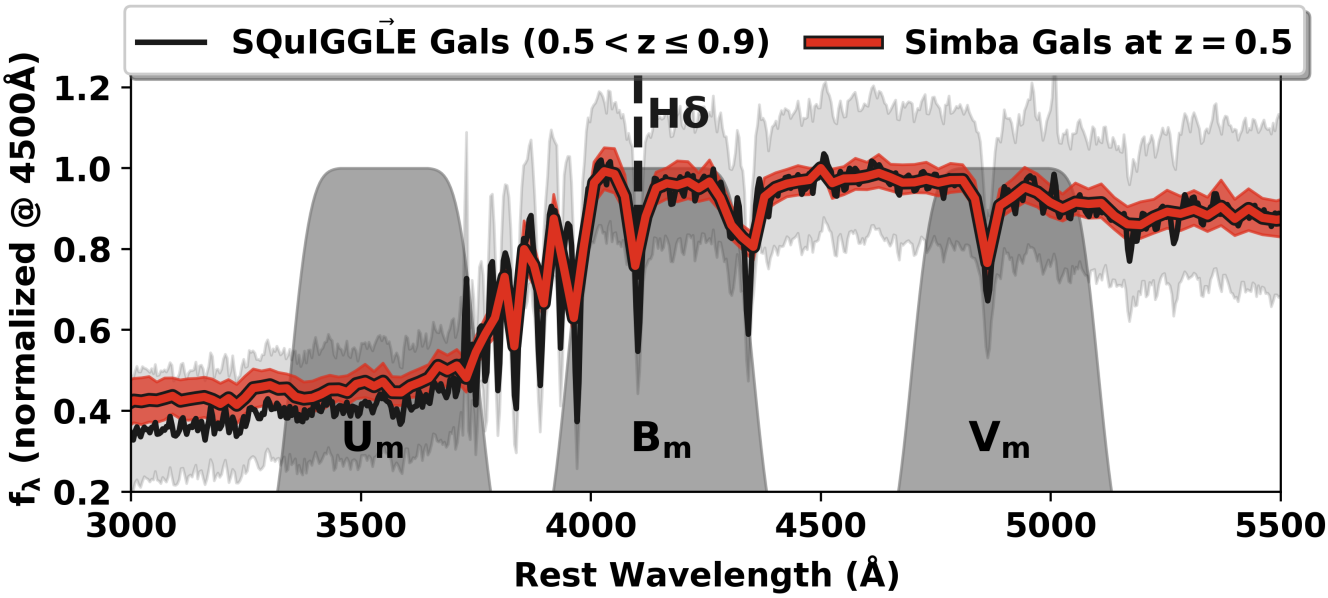


Figure 15. In general, SQuiGG$\vec{L}$E galaxies are redder than those UBV-selected (Eq. 5) galaxies from SIMBA. Spectral energy distributions (SEDs) for the two samples, stacked using the median, normalized at 4500Å, and surrounded by a shaded region indicating the 16th-84th percentile ranges are shown above. The black line shows the result of ∼1,300 stacked SQuiGG$\vec{L}$E galaxies from $z = 0.5 - 0.9$, while the red line shows the combined stack of 72 UBV-selected SIMBA galaxies at $z = 0.5$. Additionally, we show as gray shaded regions the synthetic rest-frame U_m, B_m, and V_m filters used to calculate the quantities shown in the left-panel of Fig. 14. Finally, we indicate the location of the Balmer Hδ absorption line via a dashed vertical black line at $\lambda = 4101.734$Å. We see here that in comparison to SQuiGG$\vec{L}$E galaxies, the UBV-selected systems in SIMBA show a weaker Balmer break and stronger UV emission, suggesting that their stellar populations are more strongly influenced by recent star formation and therefore contain a larger fraction of young, hot, and massive stars.